Spring 2023

# PRELIMINARY VALIDATION OF A HIGH-PERFORMANCE ELECTROTHERMAL MODEL OF AN ELECTROMAGNETIC HEATING SYSTEM

Jeremiah Vardaman
*University of New Hampshire, Durham*

# PRELIMINARY VALIDATION OF A HIGH-PERFORMANCE ELECTROTHERMAL MODEL OF AN ELECTROMAGNETIC HEATING SYSTEM

BY

Jeremiah Vardaman

Bachelor of Science in Electrical and Computer Engineering,

University of New Hampshire, 2018

THESIS

Submitted to the University of New Hampshire

in Partial Fulfillment of

the Requirements for the Degree of

Master of Science

in

Electrical Engineering

May, 2023

This thesis has been examined and approved in partial fulfillment of the requirements for the degree of Master of Science in Electrical Engineering by:

**Thesis Director: Dr. Kent Chamberlin**
Professor and Chair Emeritus of the Department
(Electrical and Computer Engineering)

**Dr. John LaCourse**
Professor and Chair of the Department
(Electrical and Computer Engineering)

**Dr. Richard Messner**
Associate Professor of the Department
(Electrical and Computer Engineering)

**Mr. Joseph Burke**
PE and Manager of Research & Technology
(Watts Water Technologies)

on April 24, 2023.

Original approval signatures are on file with the University of New Hampshire Graduate School.

# Acknowledgements

This research was made possible by the support and funding of Watts Water Technologies' research grant to the University of New Hampshire Department of Electrical and Computer Engineering.

I am extremely grateful to my thesis advisor, Dr. Kent Chamberlin, for his guidance and support throughout the process of research and thesis writing. Dr. Chamberlin has encouraged me throughout the years and imparted many lessons, both in the classroom and professional setting. It has been a pleasure working with him.

Many thanks to Mr. Joseph Burke of Watts Water Technologies for his enthusiasm and problem-solving skills during our many weekly meetings. His energy and helpful attitude throughout the research was greatly appreciated.

I would like to thank Dr. John LaCourse and Dr. Richard Messner for serving on my committee. I am appreciative of their time and thoughtful edits on this thesis.

I wish to thank Steven Philips and Alhussein Al-Jawad for sharing their time and knowledge.

Many thanks to my friends, family, and peers for their encouragement and support to follow through and pursue this degree to its completion.

Finally, I want to thank my incredible fiancée for her continuous support, endless patience, and for believing in me.

# Table of Contents

# List of Tables

# List of Figures

# Abstract

PRELIMINARY VALIDATION OF A HIGH-PERFORMANCE ELECTROTHERMAL MODEL OF AN ELECTROMAGNETIC HEATING SYSTEM

by

Jeremiah Vardaman

University of New Hampshire

To aid in the design and development of an electrical induction thermoplastic pipe-fusion product, Ansys HFSS, an electromagnetics simulation package, and Ansys Mechanical, a thermal dynamics simulation package, were used to simulate a model of the pipe-fusion product. HFSS estimated the currents induced in conductive susceptors embedded in the pipe fitting. Then, Mechanical estimated temperature dynamics on the susceptors as a function of the induced currents. The heat generated by induced currents on the susceptors increases temperatures in the vicinity of the region to be fused. The increased temperature of the thermoplastic facilitates a pipe fuse. The simulation results were compared to thermal measurements of the physical system. Thermocouples and infrared cameras were used to acquire thermal measurements of the pipe fusing process, while a micro computed tomography (μCT) scanner was used for internal imaging of fitting components' movement before and after the fusing process. Adjustments to the HFSS solution parameters were needed to achieve reasonable agreement with the physical measurements. In the final analysis, comparison against measured data resulted in a simulation that is sufficient to serve as a meaningful tool in the development of new pipe fusion products. This thesis provides details on how the model of the pipe fusion system was created and how the results of the model's simulation were validated against thermal measurements of a physical electrical induction pipe-fusion system.

# Chapter 1: Introduction

## 1.1 – Pipe Fusion via Electromagnetic Induction

Electromagnetic induction is a fundamental principle of electricity that describes how a changing magnetic field generates an electric current in a conductor. Induction itself does not apply thermal energy directly but induces eddy currents that heat electrically conductive objects via the Joule effect [1]. These eddy currents create heat in the same manner as an electrical current flowing through any partially conducting object, such as a resistor.

Induction heating has many uses including heating metals, annealing, welding, and other manufacturing processes. It has even been used to selectively heat and kill targeted tissue within a tumor [1]. Figure 1 shows an example of induction being used to generate heat in brass piping. Induction heating is more efficient, faster, safer, and cleaner than other forms of heating [1] [2]. The application of thermal energy via induction is also very controllable due to time delays between the application of electrical energy and the temperature change at the induction point being very low [2]. Due to these benefits, it is a good technique for joining thermoplastic piping, which is used in many industrial applications due to its light weight and resistance to chemical reactions [3].

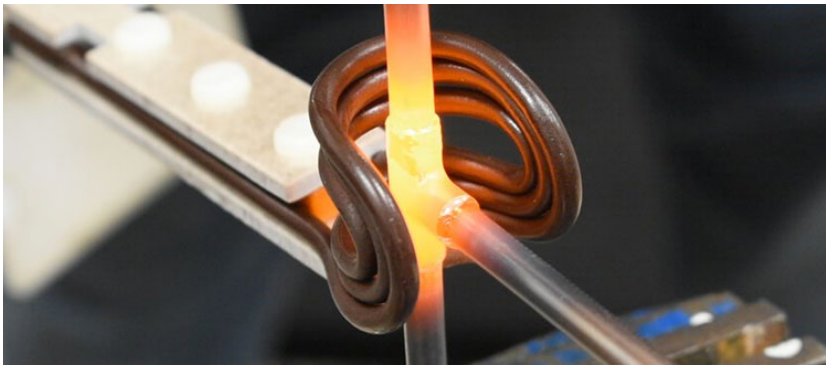

*Figure 1: Brass induction welding example [4]*

Plastic pipe sections are joined with the use of a coupler, which is a fitting that connects the ends of pipes together. Pipe ends are typically joined to the coupler via adhesive bonding, mechanical fastening, or fusion bonding which softens the plastic with heat to allow components to physically join at a molecular level due to intertwining polymer chains. When thermoplastic material is heated and becomes viscous, the polymer chains unwind and stretch out. When the material is then cooled the polymer chains wind back and link with one another to create a robust structural bond [5].

There are many ways to create a fusion bond, as detailed below in Figure 2. The fusion system used for this research thesis utilizes electromagnetic induction welding, in which an electrically conductive material, called a susceptor, is embedded in the thermoplastic material. The susceptor is heated inductively by an external, alternating magnetic-field source.

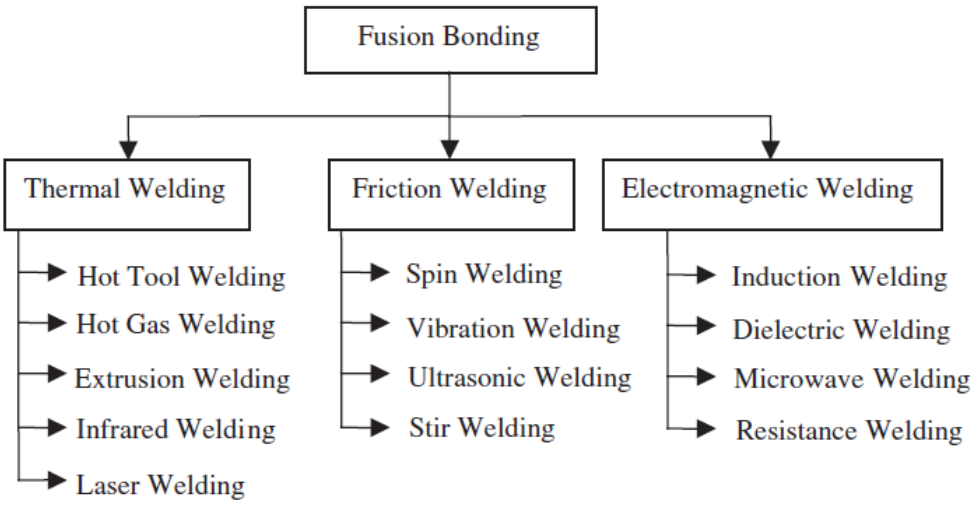


*Figure 2: Fusion Bonding Classification [3]*

Figure 3 shows an example of electromagnetic induction welding being used to generate heat at the connection of two steel shafts. An alternating current source is used to send current through the single copper loop around the shaft ends. The magnetic field around the loop induces eddy currents in the steel, which generates thermal energy and welds the two shafts together.

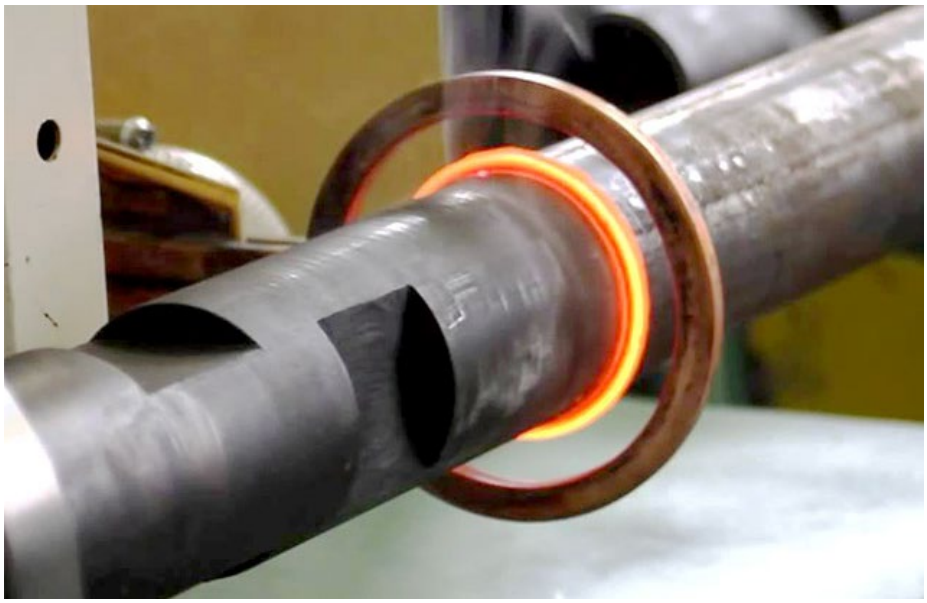

*Figure 3: Induction shaft welding example [6]*

## 1.2 – TRITON™ Pipe Fusion System

The Watts Water Technologies' TRITON™ system, shown in Figure 4, is a portable pipe fusion system that uses electromagnetic induction heating to fuse high density polyethylene (HDPE) pipes together. The system has three main components: the control unit, the fuser, and a fitting. The control unit is a radio frequency (RF) power generator controlled by an onboard microcontroller. The control unit operates in the Industrial, Scientific, and Medical (ISM) frequency band of 13.56MHz [7]. The fuser contains an impedance-matching circuit and a copper loop that can be clamped around a fitting. The fitting used is a specialized HDPE pipe coupler with steel susceptor rings embedded at all openings that accept a HDPE pipe, shown in Figure 4.

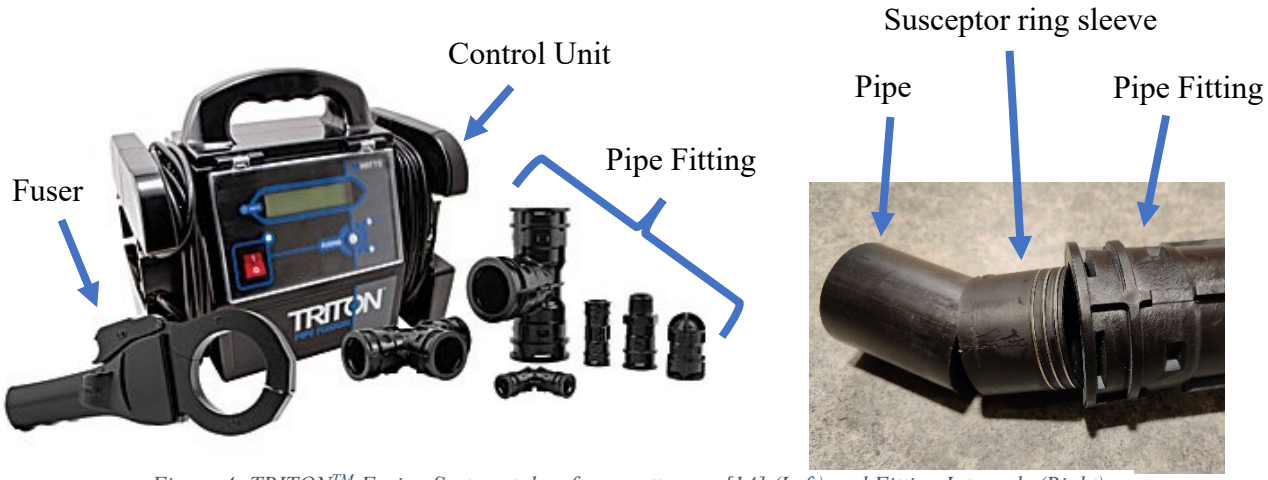


*Figure 4: TRITON™ Fusion System, taken from watts.com [14] (Left) and Fitting Internals (Right)*

During operation, the fuser is clamped around the fitting's susceptor rings. The control unit supplies an alternating current to the fuser's copper loop. This creates a time-varying magnetic field in the fuser's copper loop which inductively generates electric currents in the fitting's susceptor rings, as described by Faraday's Law. The induced currents cause the rings to

heat up and conduct thermal energy to the surrounding HDPE, which fuses the pipe ends and fitting together. This process is visualized in Figure 5.

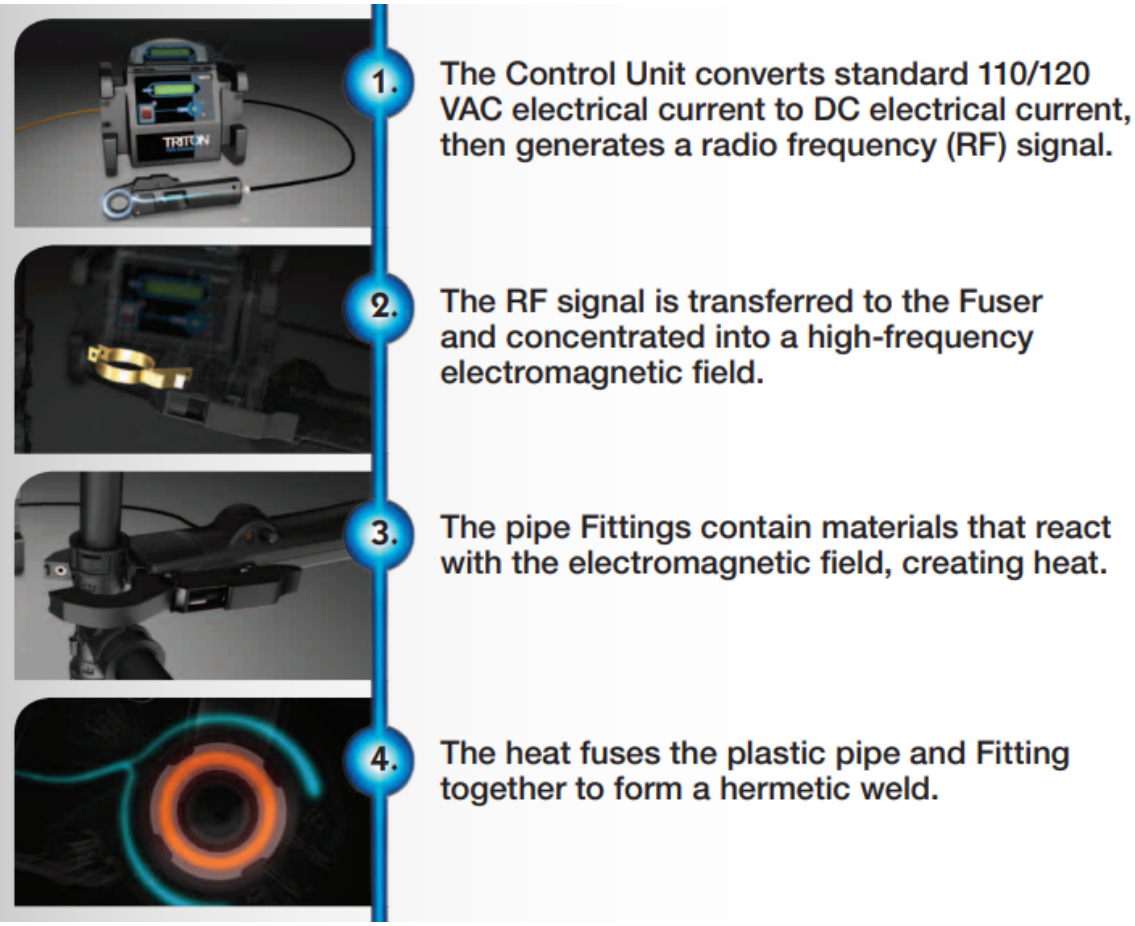


*Figure 5: How it Works, from watts.com [8]*

The TRITON™ Pipe Fusion system is the first system to use RF electromagnetic induction for plastic pipe joining [9]. The TRITON™ system was designed to be a fast, portable, and straightforward to implement in the field. This is accomplished due to its ability to heat the susceptor rings internal to a piping fitting. This makes it safer to use compared to other thermal joining methods due to the lack of exposed heating elements as the susceptor rings are fully enclosed in the fitting. Noguchi et al. (2020) show that polymer volatile organic compound

(VOC) emission increases drastically with temperature [10]. With no exposed heating element, the melted HDPE remains internal to the fitting, thereby limiting VOC emission versus an exposed heating solution.

The purpose of this thesis is to develop a simulation tool as an aid in the design of TRITON™ electromagnetic pipe-fusion products. This was accomplished by: (1) recreating the electrothermal fuse process in a computational simulation, (2) collecting measurements from the physical TRITON™ 2-inch pipe fusion system, (3) comparing the measured and simulated heating profiles, and (4) adjusting the model parameters to improve and validate the simulation.

## 1.3 – TRITON™ Fusion Simulation

A complete model of the TRITON™ pipe fusion system was created by implementing two separate simulators: Ansys High Frequency Structure Simulator (HFSS) to estimate the electromagnetic coupling between the fuser and the susceptor rings, and Ansys Mechanical to account for the heating that takes place in the rings and surrounding plastic resulting from the power delivered to the susceptor rings.

HFSS is an industry-standard, state-of-the-art, full-wave 3D electromagnetic field simulator that uses Finite Element Method (FEM) and adaptive, reiterative meshing to approximate the configuration under analysis [11]. The FEM discretizes models into a finite number of smaller and simpler elements that are interconnected. The physical aspects of each element are defined mathematically by a set of equations which are assembled to form a system of equations matrix that describes the behavior of the simulated model. The system is solved to satisfy Maxwell's Equations and the boundary conditions.

Ansys Mechanical is a FEM simulator for structural and thermal transients [12]. Ansys Mechanical is hereinafter referred to as the "thermal simulator". Figure 6 shows a snapshot of how Ansys Workbench, an Ansys workflow integration platform, links HFSS and the thermal simulator to create the complete electrothermal simulation.

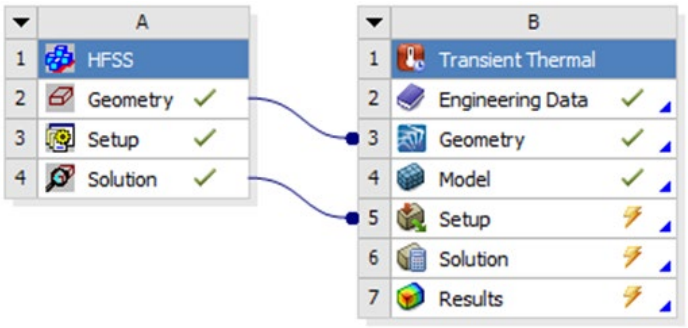


*Figure 6: HFSS and thermal simulator in Workbench*

The simulation flow is shown below in Figure 7. The input parameters to HFSS are the model, being its geometry and material properties, the current excitation port, the radiation boundary, and the FEM initial mesh seeding. HFSS simulates the induced electrical energy on the rings. The results and model geometry are imputed to the thermal simulator, which estimates the thermal energy on the rings as a result of the induced current. The conduction of thermal energy to the surrounding HDPE is then simulated, which is what facilitates a pipe fuse in the physical system.

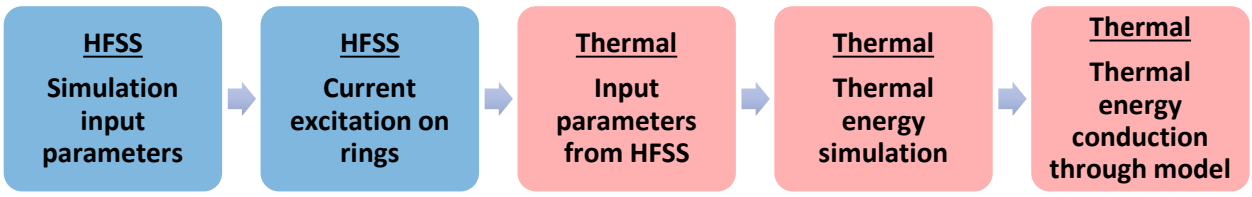


*Figure 7: The electrothermal simulation workflow*

# Chapter 2: Simulation Development

## 2.1 – HFSS Simulation

The development effort described here was performed using the standard, TRITON™, 2-inch fitting, where the parameters of that fitting, being dimensions and material properties, were used to make the model.

The fuser's impedance matching circuit was recreated in Multisim, an electronic circuit simulation software, to analyze the power loss from the matching circuit components. The Multisim $S^{11}$ reflection coefficient, which is a measure of how much signal is reflected due to an impedance mismatch, was in agreement with the measured $S^{11}$ value of the physical fuser. This agreement gave validity to the power loss calculated by Multisim. The power loss was found to be less than 3% of the total delivered power form the control unit. For the purpose of this thesis, the energy lost to the heating of the fuser wand circuit components was deemed negligible to the overall delivered power that us sent to the fuser copper loop. The HDPE plastic pipe and fitting were assumed to have the magnetic properties of free space ($\mu=\mu_0$), due to their magnetic susceptibility being very low [13]. Figure 8 shows the model geometry used.

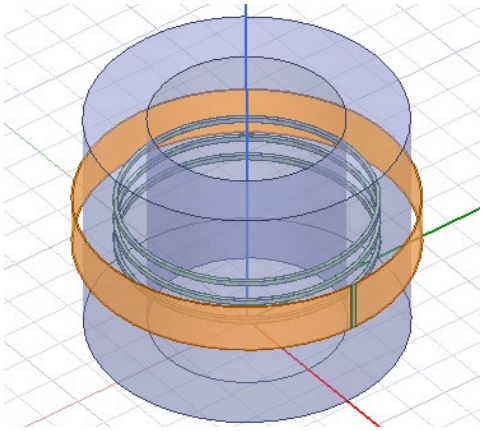

*Figure 8: HFSS Model Geometry*

To perform a simulation of the electromagnetic coupling between the fuser and the susceptor rings, HFSS solves Maxwell's Equations for the specified configuration (shown in Figure 4). HFSS uses a Finite-Element Method to satisfy both Maxwell's Equations and the boundary conditions for the configuration [14]. The boundary conditions used in the TRITON™ system were a radiation box and an excitation port. The radiation box is a defined boundary around the model that absorb outward radiating EMF waves. This boundary was implemented to eliminate reflections that would have created erroneous results due to the usage of FEM and not Method of Moments, which accounts for infinite boundaries but is less practical for simulation applications. A standard practice for HFSS is to set the radiation boundary to a quarter of a wavelength ($\lambda/4$). To meet this standard, the radiation boundary was set to be a 121 $m^2$ cube with the TRITON™ fitting model at the center, as shown in Figure 9.

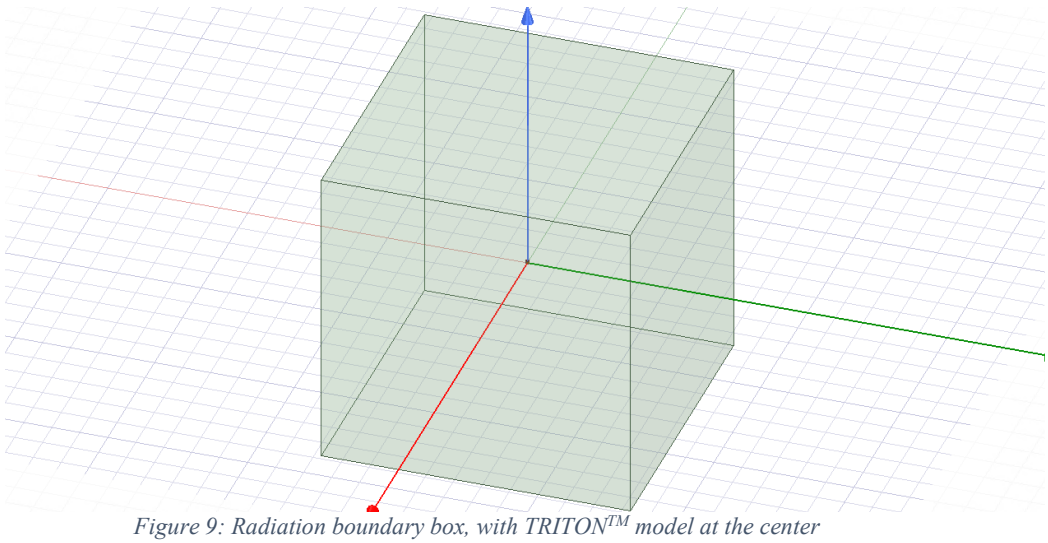

*Figure 9: Radiation boundary box, with TRITON™ model at the center*

Excitation ports are boundary conditions that provide energy flow into a model. HFSS can simulate power delivery through a variety of excitation ports, including lumped ports, wave ports, or ideal sources. An ideal current excitation port was chosen as the energy input boundary to the fuser copper loop. This was the best choice for this model due to the volumetric simulation being run. Wave and lumped ports are more ideal for transmission line or antenna modeling.

The "Arbitrary Fields Calculator" feature of HFSS was used to calculate the power delivered to each component by integrating the Poynting vector across the surface of the different geometries [14]. The simulation current source was then adjusted until the power equaled that of the average delivered power to the fuser in the physical system (i.e., 100 watts).

Figure 10 provides an annotated table showing how the power is distributed when 100 watts of power is delivered to the fuser wand for a particular susceptor-ring configuration. The efficiency is determined by the amount of power that is delivered to the susceptor rings compared to the power lost in the wand loop and the radiated power. The radiated term relates to power propagated away from the configuration as radio frequency energy. It is given by the difference between the total power delivered to the system, and the total power dissipated (i.e. 96 watts). The energy radiated is relatively small at about 4% of the total power. This is due to the copper fuse wand loop being an inefficient radiator at 13.56 kHz.

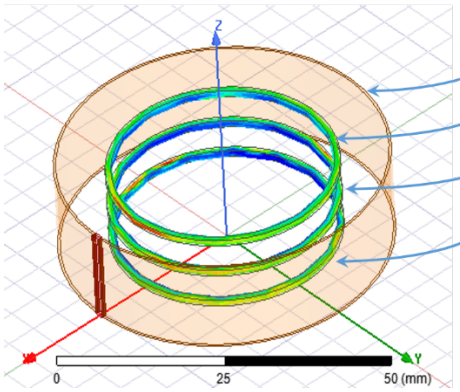


| Power to Wand Loop = 100 W | |
|---|---|
| **Conductor** | **Power Dissipated** |
| Wand Loop | 42 W |
| Susceptor #1 | 19 W |
| Susceptor #2 | 17 W |
| Susceptor #3 | 18 W |
| $P_{radiated}$ | 4 W |
| Efficiency | 54 % |

*Figure 10: Standard configuration for 2-inch fitting being simulated with carbon steel susceptor rings*

HFSS, in general, is most robust for geometry-to-wavelength ratio of 10 or greater. As model geometry decreases with respect to the wavelength of the simulated frequency, more adjustments are needed for HFSS to simulate reasonable results.

The TRITON™ system operates at 13.56 MHz, which equates to a wavelength of 22.12 meters. The components are significantly smaller at roughly one hundredth of a wavelength. Due to the large difference between model size and the wavelength, the out-of-the-box configuration of HFSS did not provide expected results. Appendix A describes several methods that were explored to explain these results; however, they did not provide meaningful improvements to the simulation. The adjustments that were successful in improving the HFSS results are described in this chapter.

An important reasonability check performed on the simulated results was to explore cases where symmetry would be expected. For example, the configuration previously shown in Figure 8 exhibits circumferential symmetry around the rings as well as symmetry in the height axis. Asymmetric simulated current excitation would have indicated errors with the solver setup.

The blue line in Figure 11 shows the initial simulated surface-current density around the circumference of the susceptor ring before any optimizations. The current density showed asymmetries and discontinuities and had a standard deviation from the mean of 612 A/m$^2$. These indicated errors in the modeling process that would negatively impact the heating profile of a simulated fuse.

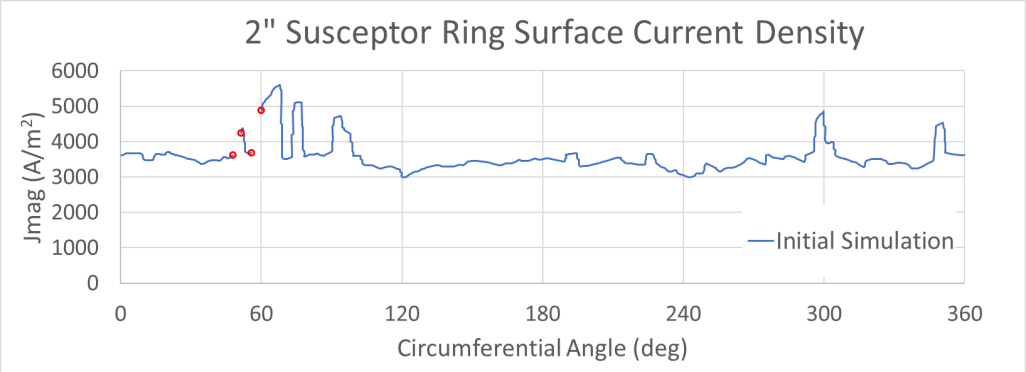


*Figure 11: Initial Simulated Surface Current Density*

As noted earlier, the simulator was being operated in a geometry-to-wavelength ratio that required manual tweaking from HFSS out of the box. There are no clearly defined fixes for the type of errors evident in the blue trace in Figure 11. The first step taken to resolve the asymmetric simulation was to fine-tune the resolution of the FEM mesh.

HFSS discretizes the model geometry into elements, or cells, that compose the FEM mesh. An example of this can be seen in Figure 12. The properties of each cell are homogenous within the cell. As such, the size and number of mesh cells affects the simulated results. How the mesh is setup is critical to the performance and accuracy of the simulated results. HFSS automatically generates the mesh based on the geometry of the model and the operating frequency. However, the TRITON$^{TM}$ model required manual input in addition to the automated mesh generation. The first adjustment was to set the initial mesh cell size to the smallest value

and to use curvilinear cells, which is a higher order cell geometry that better approximates the curved geometries of the model. Another adjustment needed was to increase the approximation densities of both the volumetric mesh and surface mesh. These manual adjustments helped to seed the initial mesh such that the adaptive meshing algorithm could better solve the solution.

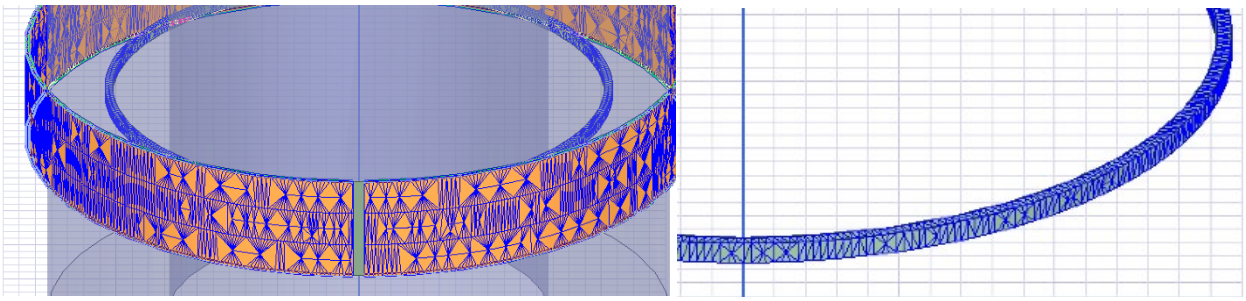

*Figure 12: HFSS Fuser Loop Mesh (Left) and HFSS Susceptor Ring Mesh (Right)*

The general HFSS simulation flow is shown in Figure 13. A more complete flow diagram of the HFSS simulation can be seen in Appendix B. A full solution pass, which is the solution of the FEM system of equations, is run on the initial FEM mesh for the model. HFSS then runs an adaptive meshing algorithm that sub-divides the cells around the largest electromagnetic field gradients and edges of the model geometry. This sees a decrease in cell size and an increase in the number of cells in the mesh. Another full solution pass is performed on the new mesh. The mesh is always refined before each solution pass.

The S-parameters, which describe the amplitude and phase of the electromagnetic field at the input and output boundaries of the model, are also calculated after each solution pass. The delta-s value is the difference in S-parameter magnitude between consecutive passes. The maximum delta-s value is the criteria used to determine when the simulation has reached convergence, or completion. The simulation has converged once a solution pass after a mesh refinement ceases to see a change in the delta-s value that is greater than the defined maximum

delta-s value. By default, the maximum delta-s is set to 0.1, which is a 10% change in the delta-s value. It was found the maximum delta-s needed to be adjusted down to 0.005, which is 0.5%. Setting a lower maximum delta-s value ensured the simulation reached a more stable solution by running more full-solution and adaptive mesh passes.

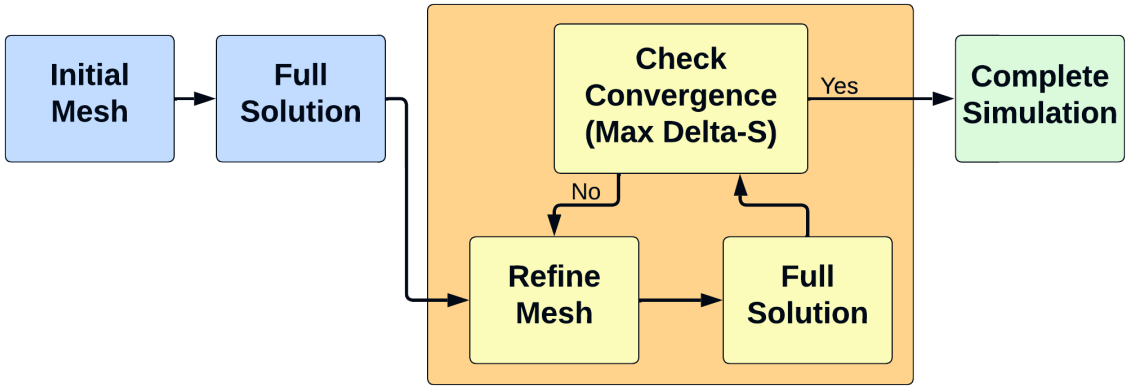


*Figure 13: HFSS simulation flow*

In addition to the delta-s parameter, the simulation can be set to a minimum number of solution passes and a minimum number of converged solution passes. Increasing these allows HFSS more simulation passes to reach convergence, as well as confirming the simulation has reached convergence.

Finally, the solver dimensions, called the Model Resolution Length, were changed from millimeters to decimeters to help account for the geometry to wavelength ratio. Changing the solver to a slightly larger resolution allowed the simulation to converge more easily while still leaving enough dynamic range to resolve the smallest geometries in the model. Solver dimensions of millimeters caused the solver to perform many more solution passes and would often not reach convergence.

These changes resulted in longer solution times and increased computer resource usage, but they also resulted in the symmetric surface current density shown by the red line Figure 14. These results show a reasonably uniform surface current density with no significant discontinuities and a standard deviation from the mean of 133 A/m$^2$, which was a 78% reduction. Thus, the systematic symmetry issues within HFSS were identified and resolved. The simulation also converged to a higher surface current density value than the initial results, suggesting that the previous results were not reaching the correct level. The revised simulated surface current density was not perfectly flat but maintained computational noise due to the model geometry-to-wavelength ratio. This noise was deemed acceptable for this research due to finding reasonable simulated-to-measured temperature comparisons, as shown in Chapter 3.4. The noise is shown to not affect the overall temperature profile of a simulated fuse.

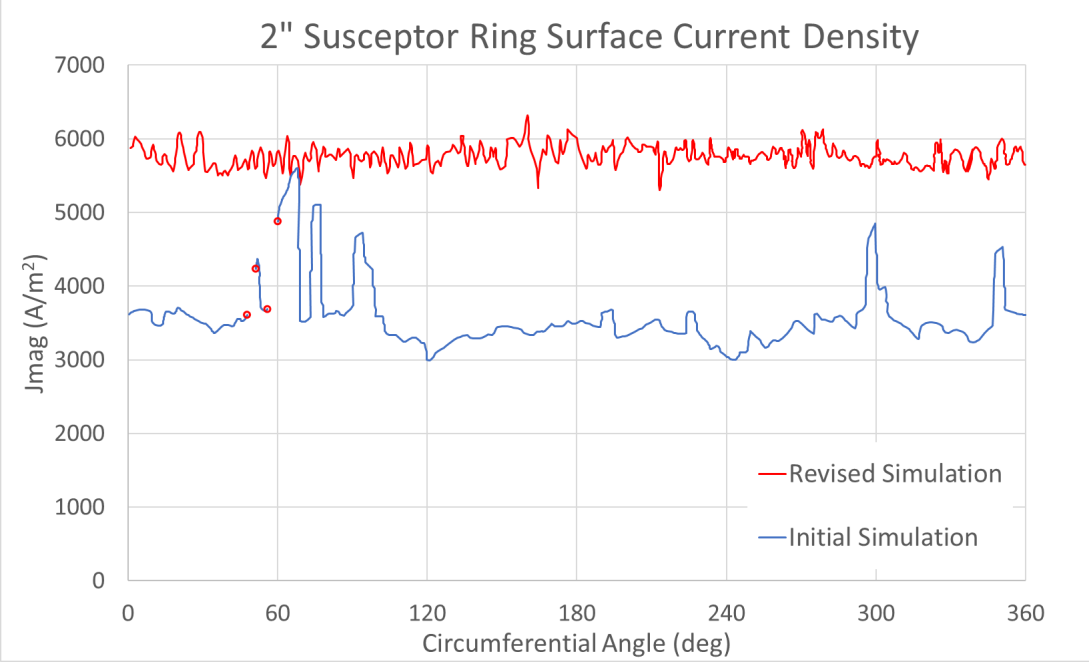


*Figure 14: Initial and revised simulated surface current densities*

## 2.2 – Thermal Simulation

While HFSS was used to simulate the induced current in the susceptor rings, the thermal simulator was used to estimate the thermal energy from the simulated current on the rings.

The model geometry and energy flux density on the susceptor rings were imported from HFSS. The thermal simulator used the HFSS-calculated energy flux to define how much thermal energy radiated from the susceptor rings. This system-to-system integration was managed internally via Workbench, so no user intervention was needed to port HFSS output data to the thermal simulator. This created a single, cohesive simulation.

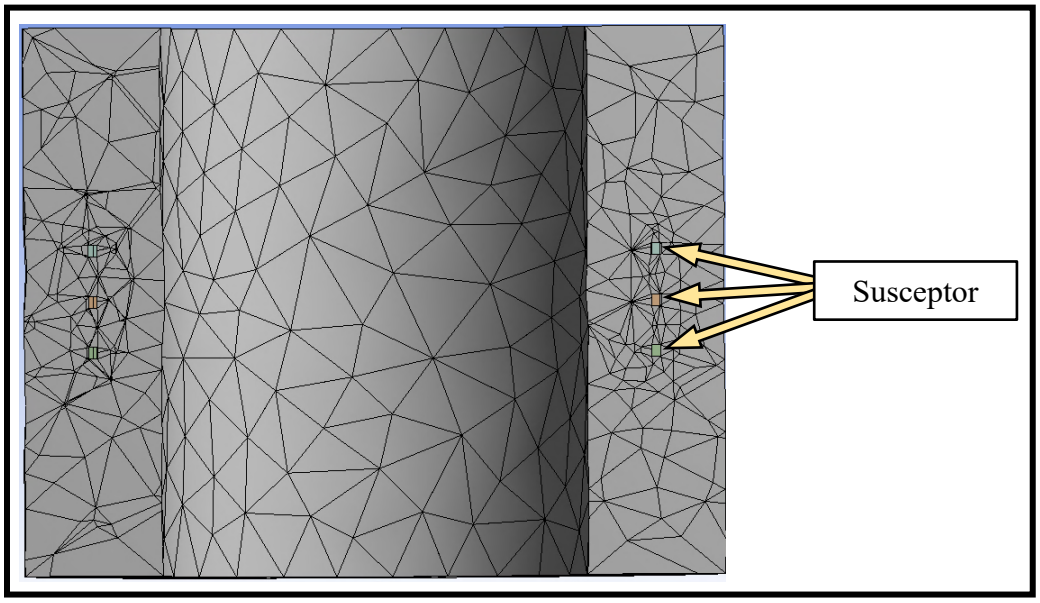


*Figure 15: Thermal simulator Finite-Element Meshing example*

As with HFSS, the thermal simulator discretizes the model geometry into mesh cells for the FEM solver. Figure 15 shows an example of the meshing in the thermal simulator. The area around the susceptor rings experiences the largest thermal gradients and therefore contains the densest mesh with smaller cells. Similar to the adjustments that were required in the HFSS model, adjustments to the mesh in the thermal simulator were required to achieve reasonable

results. While not as drastic as the HFSS model adjustments, refining the initial mesh to smaller cells increased the accuracy of the simulated fuse temperature profiles at the expense of solution computation time.

Figure 16 shows the inner and outer faces of the pipe model geometry were defined as convection surfaces to simulate air convection. The pipe was long enough to account for sufficient thermal dissipation down the length of the pipe. Static air convection was applied to the surface. The surface convection coefficients were later determined through perturbational analysis when compared against real-world measured surface heat up and cool down times.

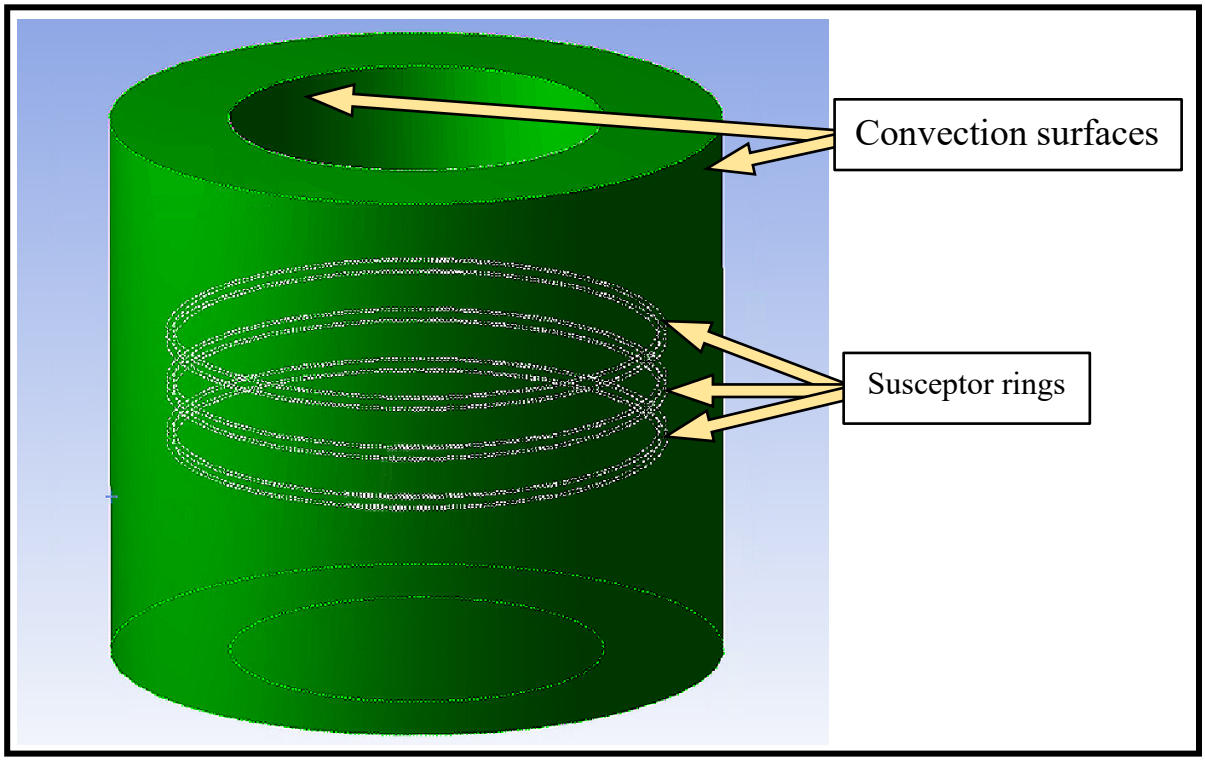


*Figure 16: Thermal simulator convection surfaces*

## 2.3 – Electrothermal Simulation

A reasonability check of the full electrothermal simulation, being HFSS and the thermal simulator, was conducted to ensure it provided results consistent with the physical system. Due to the circumferential symmetry of the susceptor rings, symmetry in the simulated heating was expected around the rings. Figure 17 show the simulated circumferential temperature for the topmost ring after a fuse cycle. The resulting temperature was considered to be sufficiently constant around the circumference. The variation seen was within range of the known computational noise. This suggested that the simulation was operating as desired and was not contaminating the results with the noise or errors within the temperature simulation solver.

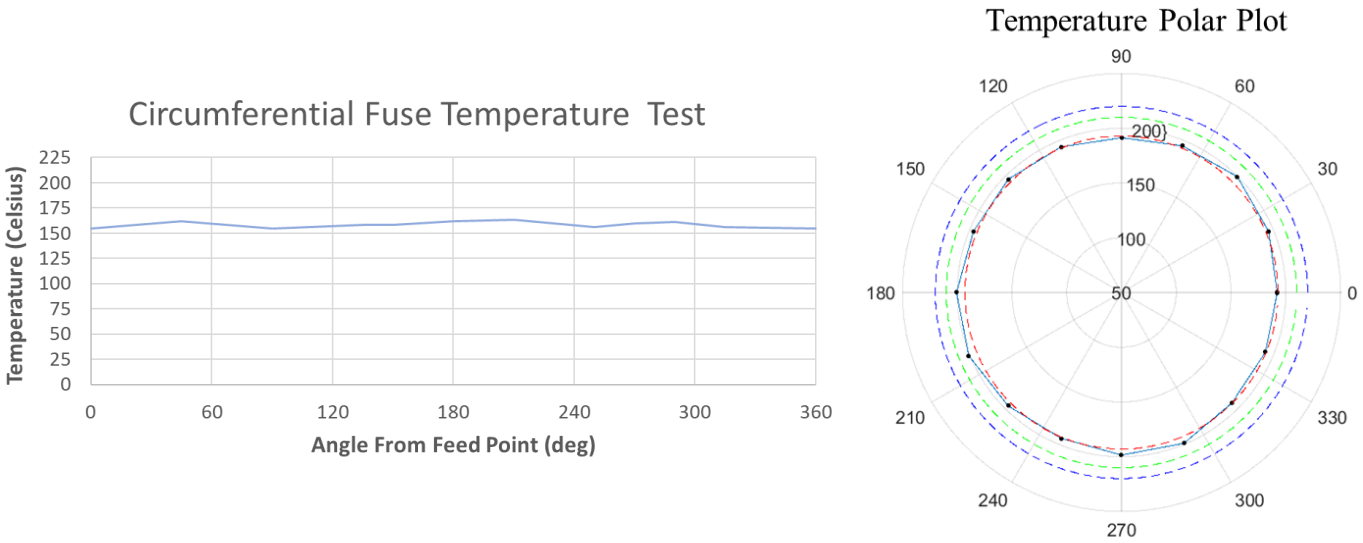


*Figure 17: Circumferential Fuse Temperature Rectangular Plot (Left) and Polar Plot (Right)*

Another reasonability check of the simulation was to look at the heating of each of the susceptor rings. Figure 18 shows the configuration of the susceptor rings, with ring 1 residing at the top of the fuser copper loop and ring 3 residing at the bottom of the loop.

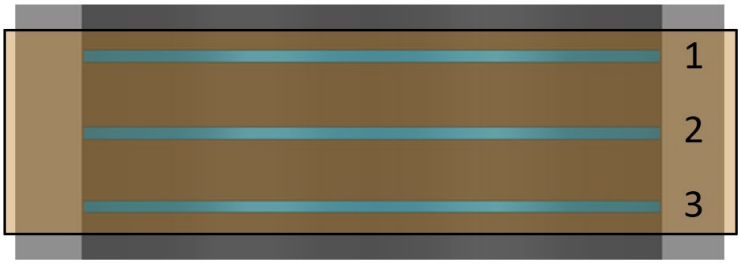


*Figure 18: Susceptor ring configuration*

Figure 19 shows the simulated surface current distribution on the wand loop. Higher magnetic flux density was expected at the edges of the copper loop due to electrical charges repelling each other towards the edge. This creates a higher concentration of magnetic field lines as they compress around the edge of the loop conductor. Due to this, more power was expected to be dissipated on rings 1 and 3 than ring 2.

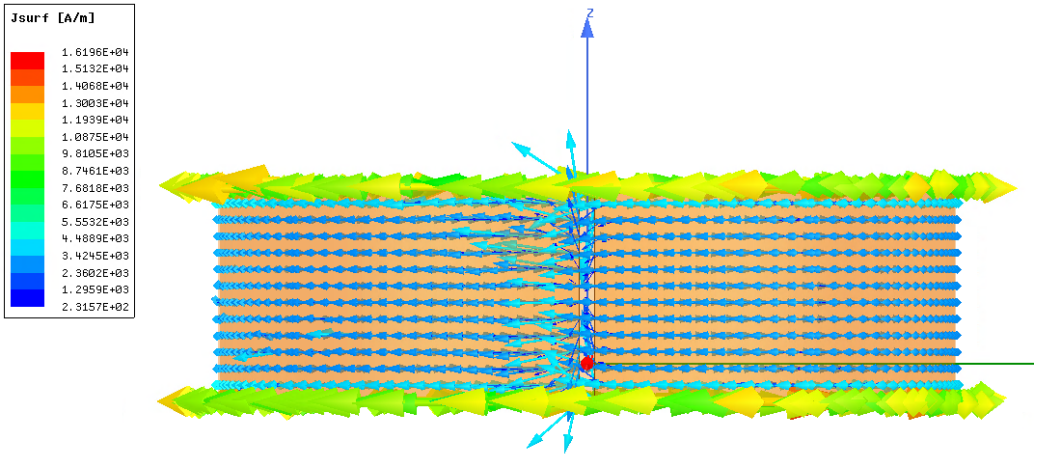


*Figure 19: Fuser loop surface current distribution shown by vector arrows*

The simulated fuse temperature profile for each of the three susceptor rings is shown in Figure 20. As expected, the outer susceptor rings rose in temperature more rapidly than the middle ring due to the outer rings residing within a higher flux region of the electromagnetic field. The middle susceptor ring experienced higher thermal energy towards the latter half of the fuse cycle due to thermal soaking between both outer rings. As both ring 1 and ring 3 heat up more than ring 2, their thermal energy conducts through the surrounding HDPE. That thermal energy combines with that of ring 2 to push the temperature of ring 2 higher. The simulated temperature of the rings was consistent with expected results and passed the reasonability check.

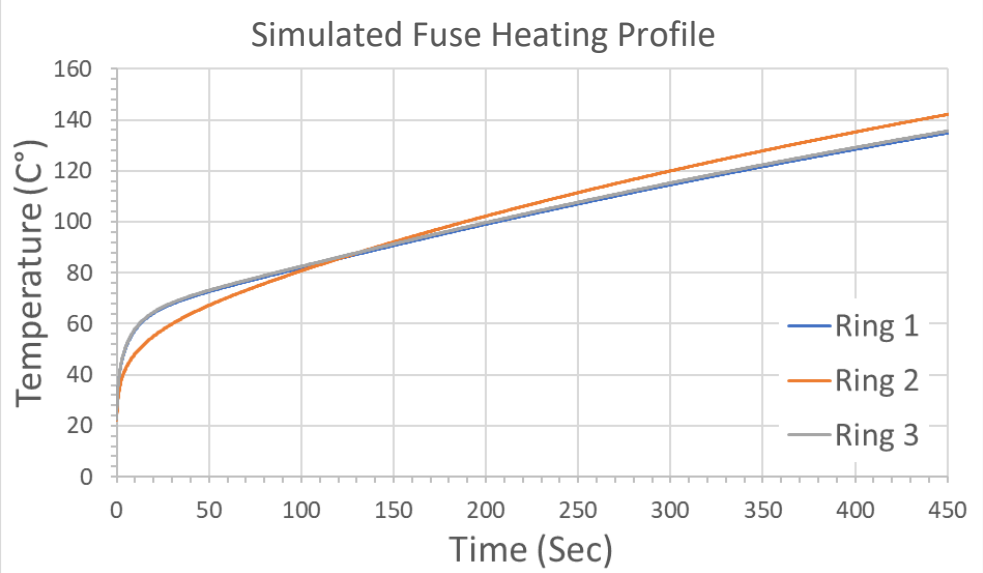


*Figure 20: Simulated Fuse Heating Profile*

# Chapter 3: Simulation Validations and Results

The simulation provided reasonable results that were in line with initial expectations. However, thermal measurements of the physical system were required to validate the simulated results. To ensure the accuracy of the measured data, experiments were conducted to measure the internal temperature of a pipe fitting during a fuse cycle.

At the onset of this research, it was discovered that the TRITON™ generator output was approximately 6% lower than the expected energy output total. The RF generator was not measuring the reflected power from the fuser wand since it was not utilizing its internal reverse-coupled wattmeter. Due to this, the generator was using only the forward-coupled wattmeter and was not delivering the intended RF wattage to the fuser wand. A fix for this was implemented in the onboard PIC18F2520 microprocessor code, so the system could correctly compensate for both forward and reflected power. Appendix C details the steps taken for measuring output power and applying the microprocessor compensation routine.

## 3.1 – Measuring Fuse Temperature of the Physical System

Thermocouples are reliable and easy-to-obtain temperature sensors. They were deemed the best tool for measuring the internal temperature of a pipe during a fusing process. Thermocouples require a simple wire welder to make a head from the ends of the two wires that make up the thermocouple. Due to the thermocouples becoming permanently trapped in fused fittings during the joining process, each pipe fitting fuse measurement required a new thermocouple. The findings presented in Appendix D show the thermocouple-to-thermocouple

accuracy and reliability to be acceptable for the research presented in this thesis. A National Instruments 9211 Thermocouple Input Module was used to measure and convert thermocouple voltage to temperature. It logged time-based readings via the software LabView, a graphical interface for data acquisition and processing.

HDPE does not conduct heat quickly, nor linearly. Due to this, thermal measurements from the exterior of the fitting did not correlate well with the modeled data of internal fuse. There was a considerable time delay when comparing the measured external temperatures to the modeled internal temperatures due to thermal conduction to the outer surface of the fitting. This latency introduced uncertainty into the validation process. To address this uncertainty, thermal measurements were made internally at the surface of the susceptor ring.

Two methods were explored for how to insert a thermocouple into the fittings. The first method was to drill a hole horizontally from the face of the fitting to the topmost susceptor ring. It was thought, once inserted, this method would place a thermocouple right at the outer face of a susceptor ring to allow for accurate temperature measurements. However, this approach introduced appreciable variability in placement of the thermocouple.

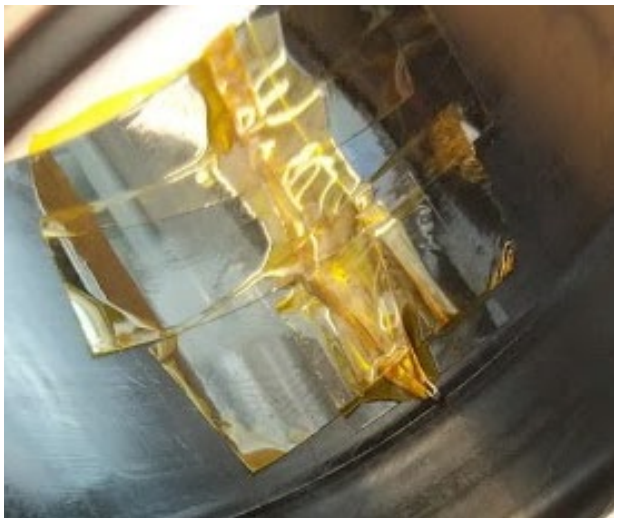

*Figure 21: Thermocouple on inside susceptor ring sleeve*

The second method explored was to place a thermocouple vertically on the susceptor ring sleeve by taping the thermocouples to the inner surface of the susceptor ring sleeve, as shown in Figure 21. Doing so placed approximately 0.33mm of HDPE between the thermocouple and the susceptor ring. Images taken with a µCT scanner, such as the one shown in Figure 22, confirmed this method was repeatable and, therefore, it was used for the remaining experiments described in this thesis. Appendix D details the thermocouple measurement process in more detail.

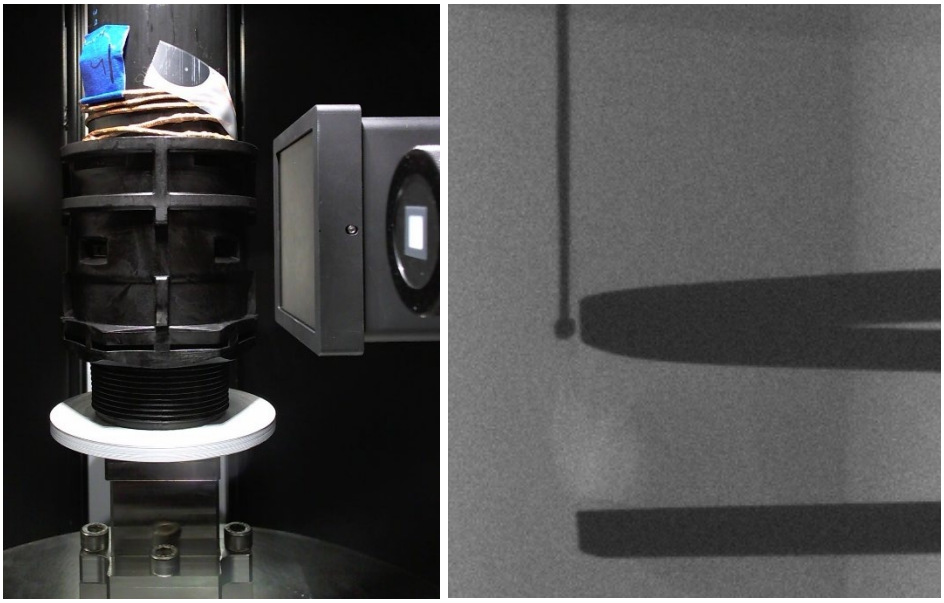

*Figure 22: Fitting in µCT scanner (left) Scan of Thermocouple Inserted into Fitting (right)*

Repeated fuse measurements of a single, virgin fitting are shown in Figure 23. The first fuse cycle reveals a sharper temperature profile; however, subsequent fuse cycles are shown to have a smoother temperature profile. This is likely due to the complex semi-crystalline structure of the HDPE polymers (Appendix E) and air gaps between fitting components (Appendix F).

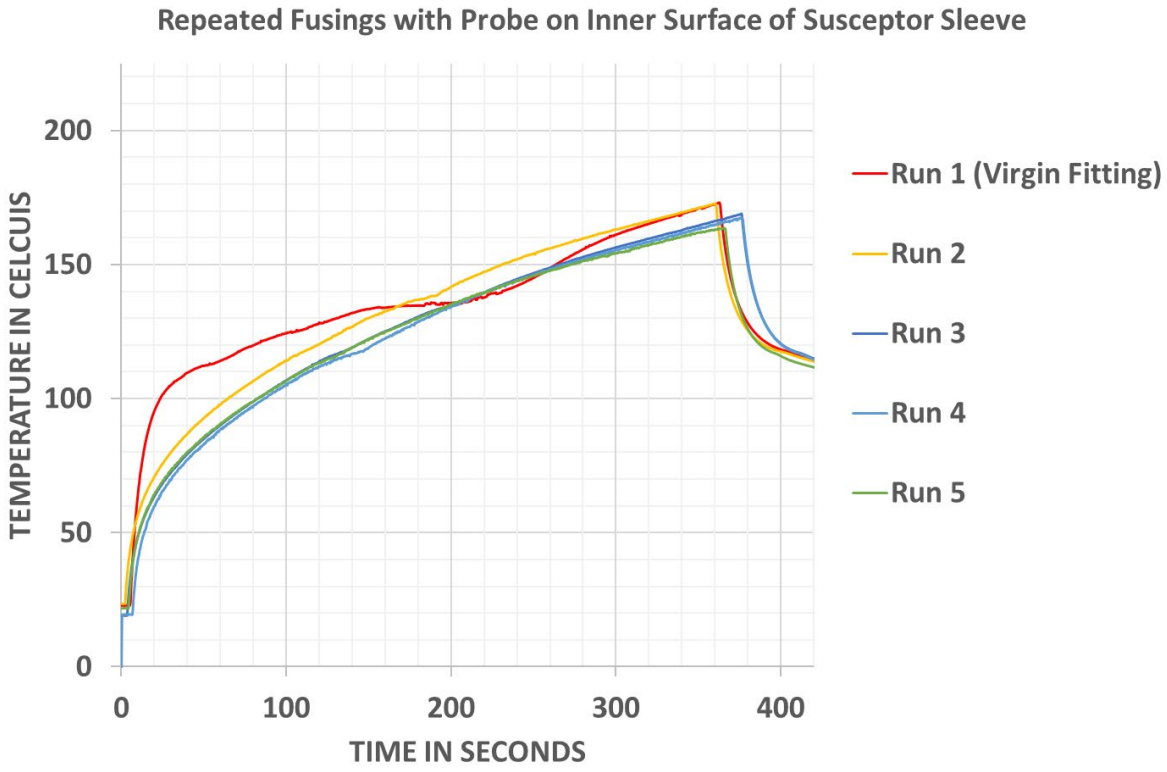


*Figure 23: Measured fuse with thermocouple on inner surface of susceptor ring sleeve*

## 3.2 – Comparison of Physical and Simulated Temperatures

Shown in Figure 24 is a plot of the preliminary simulated fuse temperature overlaid with the physical measurement shown in Figure 23. The degree of agreement between the measured and preliminary simulation data was not sufficient, which led to further analysis.

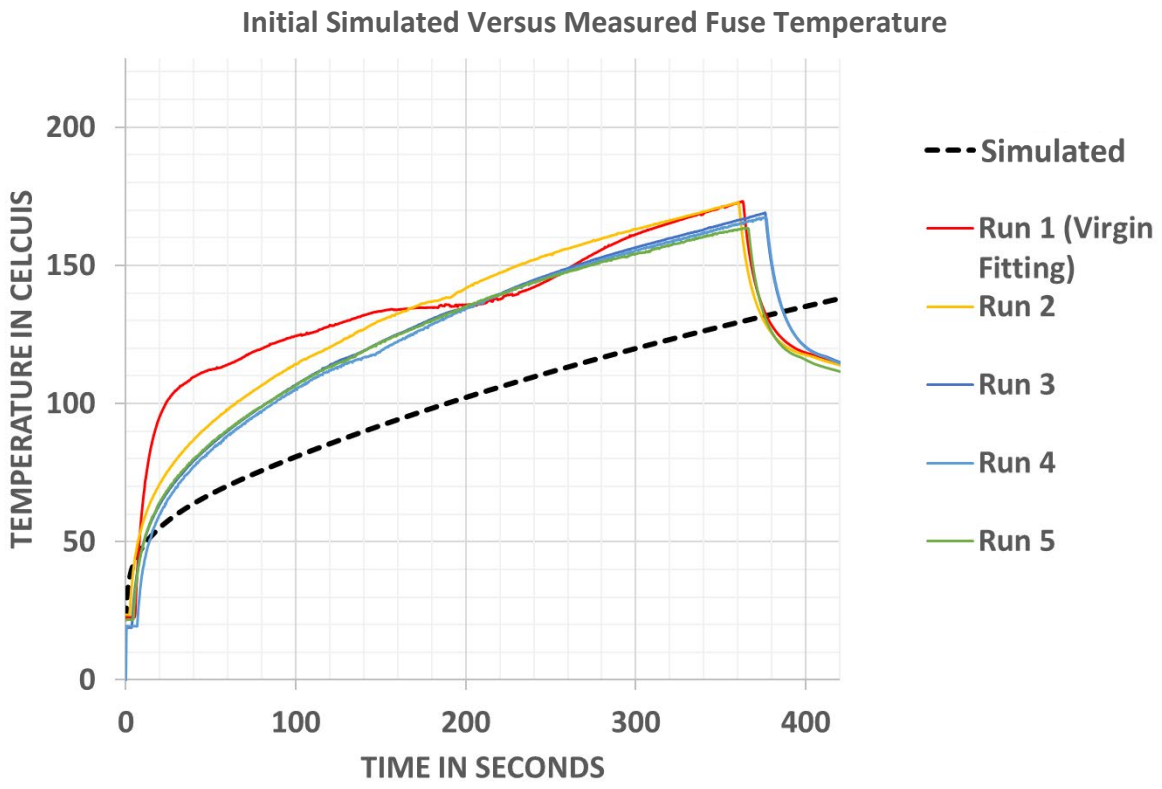


*Figure 24: Initial Simulated Versus Measured Fuse Comparison*

To provide validation for the thermocouple measurements, temperature measurements were taken using an infra-red (IR) camera. Thermocouple, IR, and model results were obtained for the canonic case of a section of pipe that had been heated and then allowed to cool as shown in Figure 25. The close agreement shown between the results is evidence that both measurement approaches and the thermal simulator were working properly. Compared to the example shown in Figure 24, this example did not involve the coupling of energy into the heating process. This finding led to a reevaluation of the energy coupling mechanism in the simulation process.

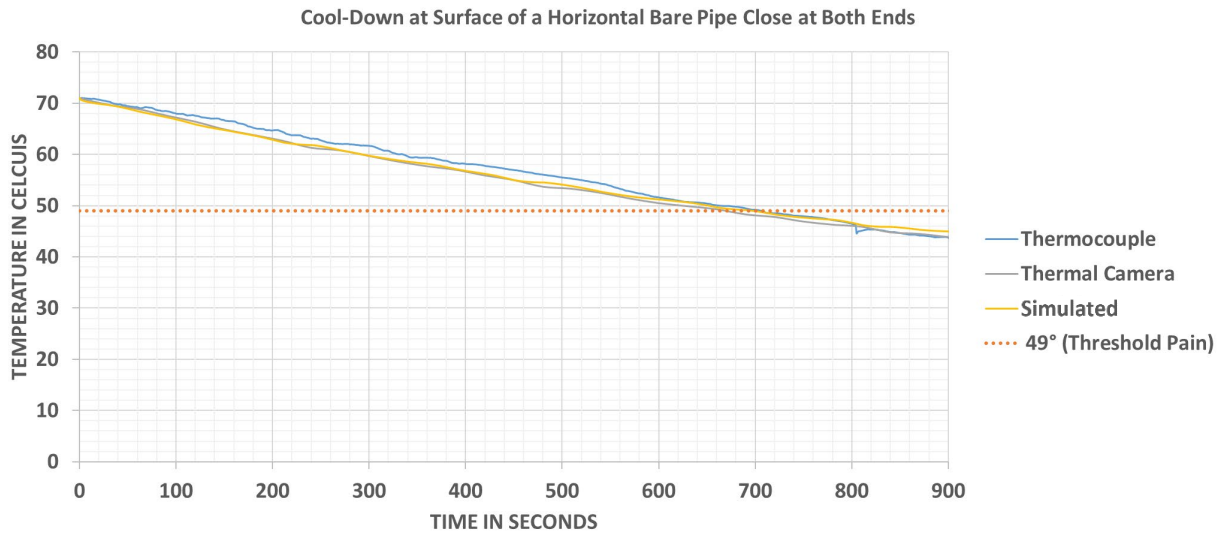


*Figure 25: Measured and Simulated Cool-Down Comparison*

It was found that the simulated fuse cycle was sensitive to the conductivity of the susceptor rings in the fitting. Varying the ring conductivity value changed the efficiency of the fuse process and, therefore, changed the thermal profile of simulated fuses. The efficiency of the fusing process is the power dissipated in the susceptor rings divided by the total power delivered to the wand loop. While it was recognized there were other loss mechanisms in the fusing process, such as losses in the electrical components and stray radiation, the resistances of the

conductors comprising the wand loop and the susceptor rings were found to be the most significant loss mechanisms. Being composed of steel, the susceptor rings were much more resistive than the copper wand loop.

The equation for electrical resistance as a function of resistivity ($\rho$) can be translated to be a function of conductivity ($\sigma$), susceptor ring length ($\ell$), and ring cross-sectional area ($R$). The equation can be rearranged to find conductivity given known resistance, length, and area of the susceptor ring, as shown in *Equation 1*.

$$R = \rho\left(\frac{\ell}{A}\right) \quad \rightarrow \quad R = \frac{1}{\sigma}\left(\frac{\ell}{A}\right) \quad \rightarrow \quad \sigma = \left(\frac{\ell}{RA}\right) \tag{1}$$

*Equation 1: Electrical Conductivity*

The power dissipated in the susceptor rings changes if their conductivity is varied. If the resistance is infinite ohms, and the conductivity is zero Siemens, no power would be dissipated on the rings and the efficiency would be 0% due to no heating generation. Conversely, if the resistance is zero ohms, and the conductivity is infinite Siemens, still no power would be dissipated on the rings. Again, no heat would be generated and would result in an efficiency of 0%. Obtaining zero efficiency at both extremes of the conductivity range implies there is some value of conductivity that will provide an optimal efficiency for the fuse process.

The 2-inch fitting model in HFSS was used to run a perturbational analysis on susceptor ring material, resulting in the plot shown in Figure 26. The simulated results showed there was, in fact, an ideal conductivity value.

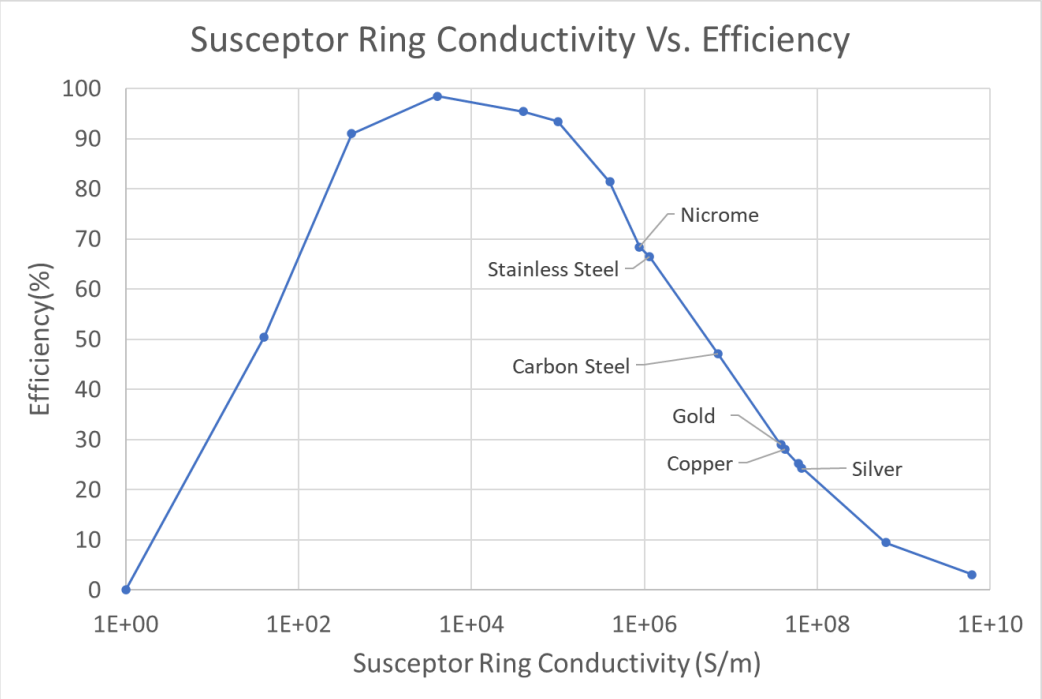


*Figure 26: HFSS simulated efficiency for the fusing process using the 2-inch fitting full-wave electromagnetics model*

To demonstrate the trends from the HFSS model were correct, a simple transformer model approximation was created to help verify the simulated results. This model also helped to explain the function of conductivity on efficiency. Please see Appendix G for more details on this transformer model approximation.

As expected, both the transformer and HFSS models show an efficiency trending towards zero for both very high and very low conductivities. The unlabeled marker points presented in Figure 26 are assumed conductivity values and do not correspond to specific known conductors. The susceptor ring conductor material used in TRITON$^{TM}$ fittings was originally thought to be standard carbon rolled steel (CRS) with a conductivity of $6.99 * 10^6$ S/m. This was the value initially used in the HFSS model. As is shown in Figure 26, a change in conductivity would have a notable change in the modeled fuse temperature profile. After some investigation, it was noted that instead of standard CRS, the susceptor rings were made of nickel-phosphorus plated 1008

CRS. The simulated fuse temperature shown in Figure 24 did not correlate well to the measured fuse temperature due to the resistance of the nickel coating not being represented in the original conductivity value. The conductivity of the nickel-phosphorus plated 1008 CRS susceptor rings was not initially known but was experimentally determined.

## 3.3 – Determination of Physical Susceptor Ring Conductivity

To determine the susceptor conductivity using Equation 1, the length and cross-sectional area of the susceptor rings was measured. To find the resistance, an experiment was setup to measure the ring resistance using a high-current 4-wire Kelvin measurement system. A high-current method was chosen to heat the ring up during the resistance measurement. Doing so allowed the thermal coefficient ($\alpha$) of the susceptor ring material to be determined. The thermal coefficient was used in a temperature-resistance relationship equation, which is detailed in Appendix F.

The 4-wire Kelvin setup is shown in Figure 27. Two variable power resistors in parallel were used to load a high-current 12 V supply to about 9 amps of current output. The current path was sent through an ammeter and a susceptor ring that had been cut in one spot to allow current travel through the entire ring. The ammeter logged the current over time while a voltmeter logged the voltage across the susceptor ring over time. 4-wire Kelvin resistance measurements are a way of measuring very small resistances without also including the resistance of the wire leads, or probes. The voltage right at the ring is measured while the current through the ring is also measured. Ohm's law is used to calculate the resistance.

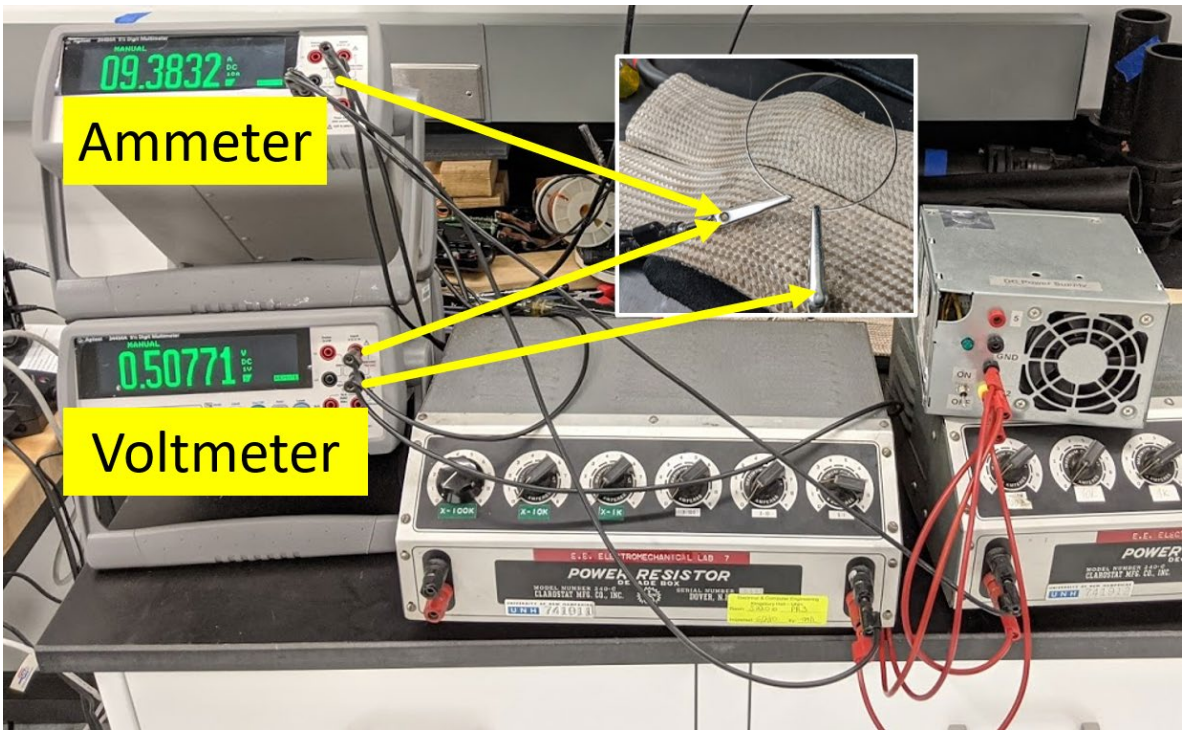


*Figure 27: 4-wire Kelvin resistance measurement setup*

The results in Figure 28 show the plot of resistance over time, as calculated from the current and voltage measurements over time. The resistance was seen to increase over time, as heat built up in the ring. The resistance plateaued around 140 seconds due to the ring thermal energy dissipation reaching an equilibrium with the thermal generation. Because this was not an adiabatic environment, thermal energy in the susceptor ring was dissipated into the surrounding air via convection. The basic equation for heat transfer is shown in (2)

Equation 2 where the heat flux ($q$) increases as the temperature delta ($\Delta T$) between the susceptor ring and the surrounding air increases given a static heat transfer coefficient ($h$).

$$\Delta T(h) = q \quad (2)$$

*Equation 2: Basic Heat Transfer*

Once the ring reached a certain temperature, the heat flux equaled that of the thermal energy generated in the ring, as seen in Figure 28. Appendix H farther illustrates the effect of convection as it shows the resistance drop when air was blown across the ring.

A susceptor ring conductivity value of $2.2 * 10^6$ S/m was calculated from *Equation 1* using the ring resistance at the beginning of the experiment in Figure 28.

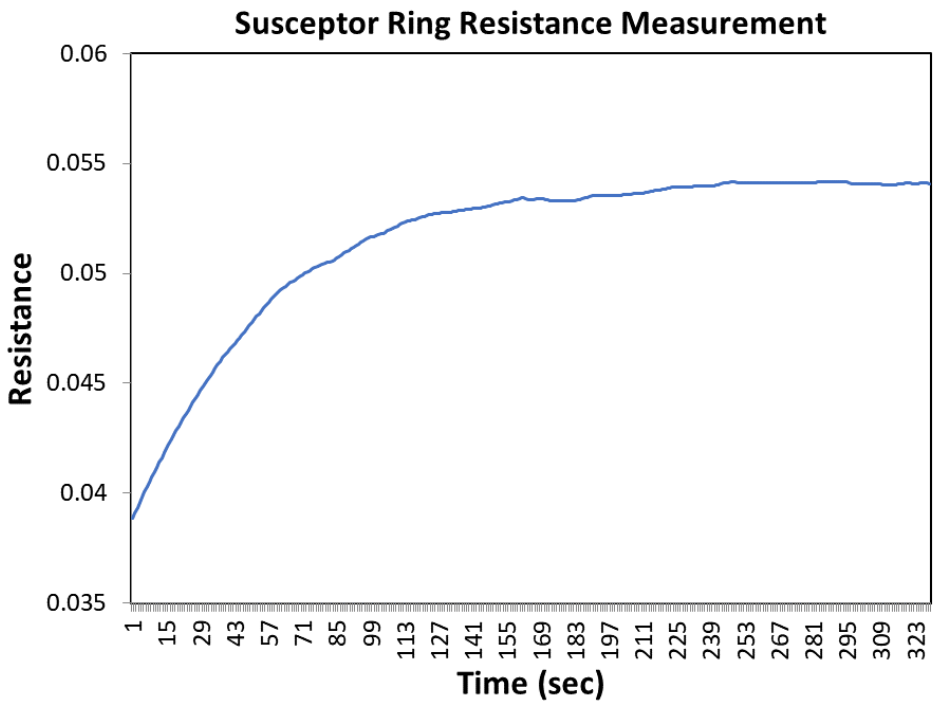


*Figure 28: Measured Susceptor Ring Resistance*

## 3.4 – Simulation Results

### 3.4.1 – Updated 2-inch Fitting Model

Figure 29 shows the measured conductivity of the susceptor rings places the simulated efficiency much higher than the original value used. As a result, the simulation was expected to provide more power to the rings and therefore see a greater increase of temperature on the rings during a simulated fuse.

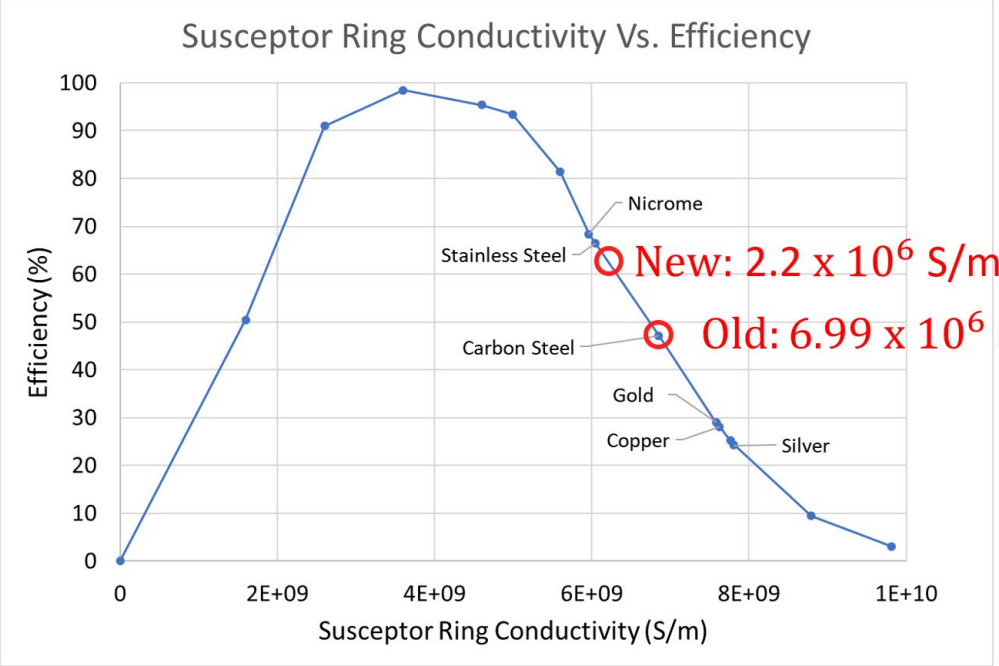


*Figure 29:HFSS simulated efficiency with old and new susceptor conductivity values*

After the susceptor ring conductivity was found for the physical susceptor ring, the corresponding value in HFSS was updated from $6.99 * 10^6$ S/m to the new $2.2 * 10^6$ S/m value. The simulated fuse temperature for the updated value is shown as a dotted black line in Figure 30. Disregarding the first fuse, the simulated fuse temperature closely matches that of the physical system. The results show they are reasonable when compared against the measured data.

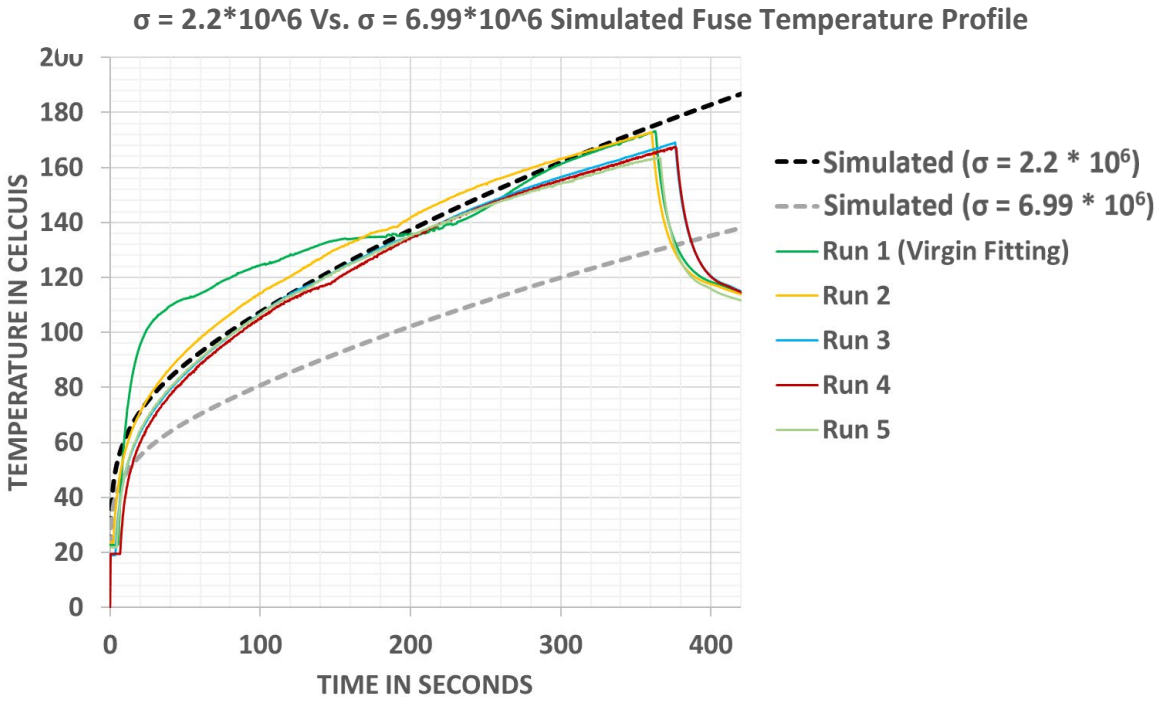


*Figure 30: Simulated Fuse at Old and New Conductivities*

### 3.4.2 – Simulation of a Theoretical 4-inch Fitting Model

The simulation of the 2-inch TRITON$^{TM}$ fitting in Ansys had been shown to provide results similar to the physical system's temperature measurements during a fuse cycle. It was then desired to test the simulation on a theoretical model of a 4-inch fitting to show how the model could be used to investigate component sizes that had not yet been realized in physical form. The theoretical 4-inch fitting model is shown in *Figure 31*. The only change in this simulation was that of the model geometry. Parameters, such as the initial mesh seeding, remained the same from the 2-inch simulation.

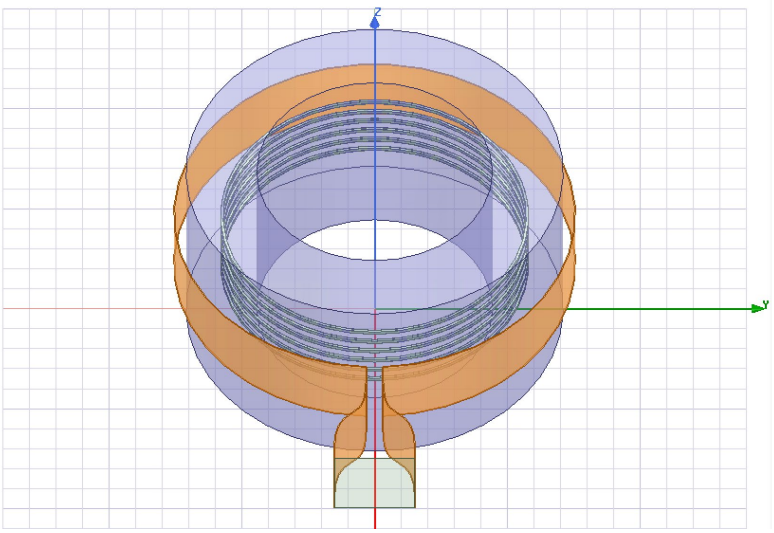


*Figure 31: 4-inch Fitting Model Design*

Figure 32 shows the 4-inch fitting model had a symmetrical current density, as was expected. This indicated the simulation was still providing expected results, like the 2-inch fitting model. The computational noise, mentioned in Chapter 2.1, was seen to scale with power input into the model.

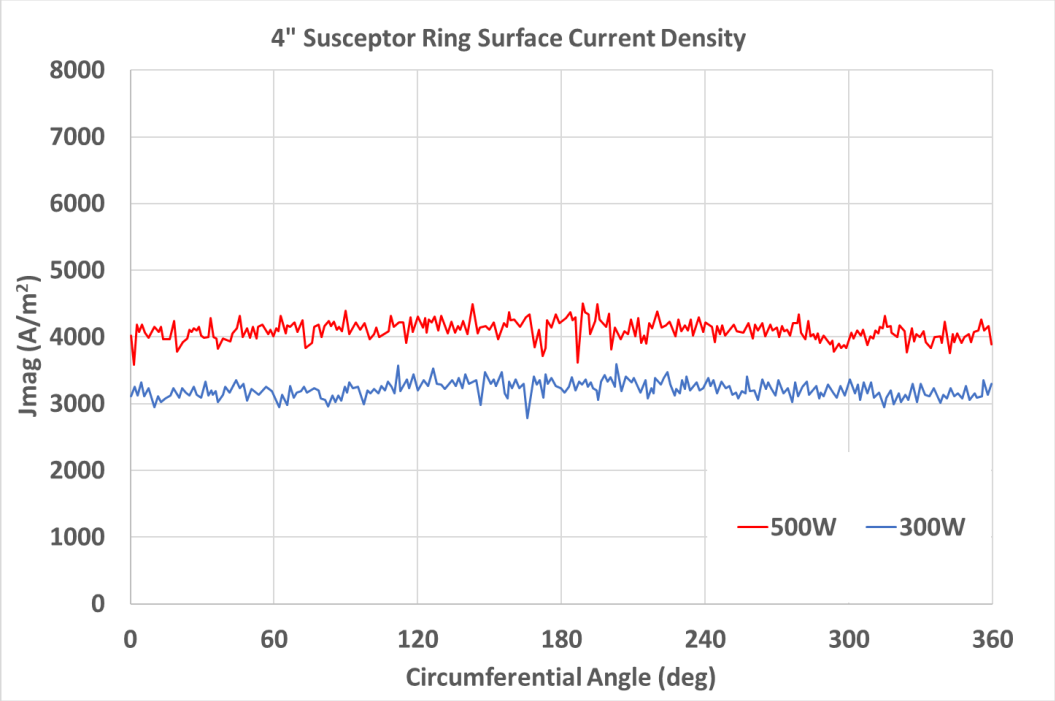


*Figure 32: 4" Fitting Susceptor Ring Surface Current Density*

Various experiments were simulated using the 4-inch fitting model. Figure 33 shows an example of a fuse depth profile for several power inputs. Figure 34 shows fuse time as a function of input power. While these plots are the result of experimental simulations, not representative of a physical system, they demonstrate the potential to provide useful information for future design work.

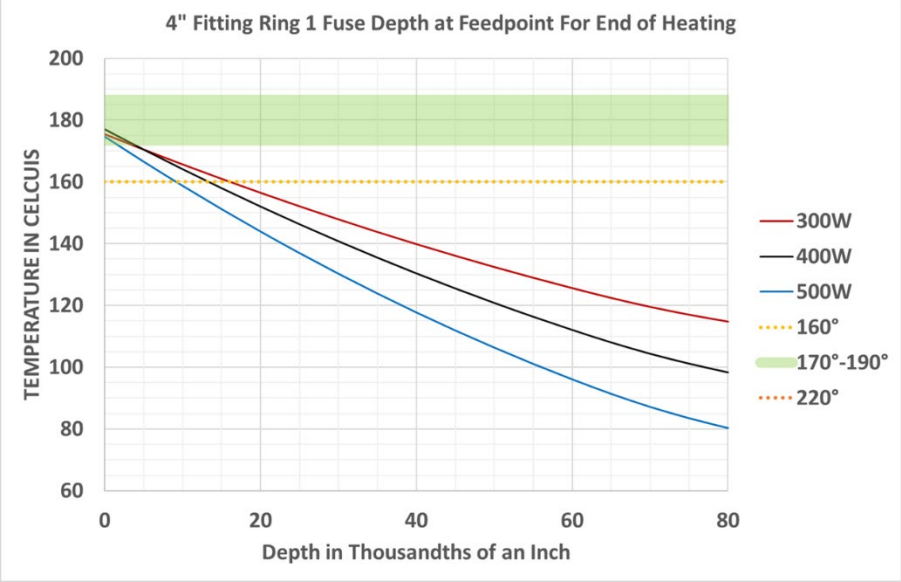


*Figure 33: 4" Fuse Depth Profile for Various Power Inputs*

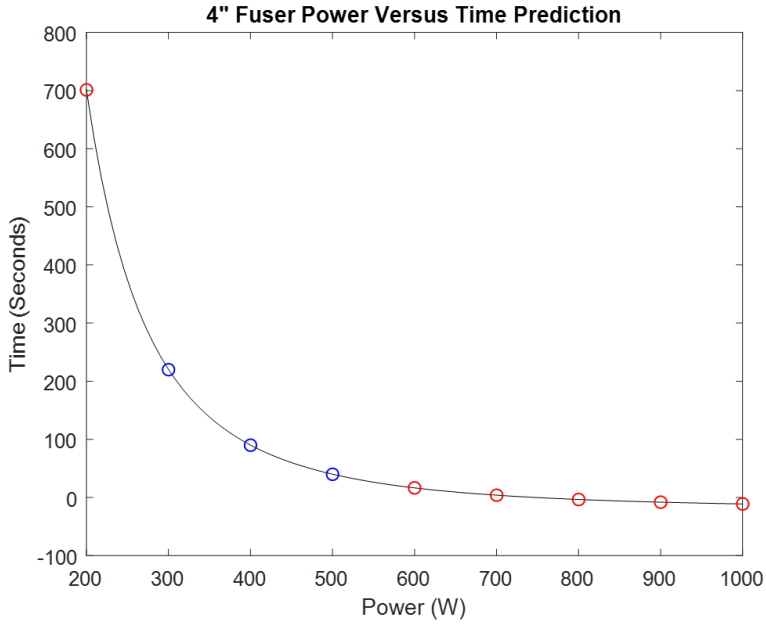


*Figure 34: 4" Fitting Power Versus Fuse Time*

### 3.4.3 – Simulation Limitations

While the simulation was determined to provide fuse temperature profile results that closely followed the physical system, it did have its limitations. Throughout the process of conducting thermal measurements on physical fittings it was noted that the heating profile was not entirely consistent from fitting to fitting, as seen in Figure G45 in Appendix F. Heating around the ring was found to be non-uniform and the heating profile between different fittings was also inconsistent. This was determined to be the result of air gaps between components in the fitting, as described in Appendix F. Air gaps create pockets of thermal insulation that were shown to change the thermal conductivity in localized areas. This caused heat to build up around the susceptor rings, which lowered the conductivity of the rings. Figure 26 demonstrates that a lower conductivity increased the efficiency of the power delivery to the ring. As the susceptor ring heated up, the resistance increased which then caused the fuse efficiency to increase. This, in turn, caused more energy to be dissipated across the susceptor ring as induced from the current flowing around the wand loop. If a localized section of a susceptor ring were to experience a higher temperature, the positive feedback in that section would cause it to become hotter than the rest of the ring.

Due to the complex properties of HDPE, as noted in Appendix E, varying internal temperatures would cause the HDPE to expand more in the hotter areas. This was found to cause susceptor ring movement during a fuse, which changed the S11 reflection coefficient and fuse efficiency. In conclusion, the localized positive feedback was hypothesized to be the cause of the measured non-uniform circumferential heating. The simulation does not account for the air gaps or the complex properties of the HDPE material.

# Chapter 4: Conclusion and Future Work

## 4.1 – Conclusion

This thesis demonstrates the successful utilization of Ansys electromagnetic and thermal simulators to develop an electrothermal simulation of the TRITON$^{TM}$ fusing process. The temperature dynamics were estimated by first calculating the currents induced in conductive susceptor ring elements embedded in the pipe fitting, and then by determining the heat generated by those currents.

Initial HFSS simulation results were analyzed for circumferential symmetry of induced current. Systematic asymmetries were found that indicated issues with the HFSS solver and model setup. It was determined that model parameter adjustments were required to improve simulation results. The first adjustment was to fine tune the initial mesh, which is used by the adaptive FEM meshing algorithm. The mesh cells were increased in density and lowered in size. Next, a lower maximum delta-s value was used to force HFSS to run more adaptive passes and full solution simulations to reach a more stable solution. The solver dimensions were also changed from millimeter to decimeter to allow the solver to better reach convergence.

Simulated fuse temperature profiles were compared to measured temperature profiles of the physical system. The simulated results were much lower in temperature than the measured and did not have reasonable agreement. It was found that the original modeled susceptor rings' conductivity did not match that of the physical susceptor rings. Because the correct value was unknown, a new value of $2.2 * 10^6$ S/m was experimentally determined. Implementing the new value resulted in a simulated fuse temperature profile that closely followed physical

measurements of non-virgin fuses. This had shown the simulation provide reasonable results that are in agreement with the physical system.

The validated simulation was tested on theoretical 4-inch fitting model geometry to demonstrate the applications to future design work for TRITON$^{TM}$ electromagnetic pipe-fusion products. Several simulated experiments were conducted with this model to show this research met the purpose of this thesis, which was to develop a simulation tool as an aid in the design of TRITON$^{TM}$ electromagnetic pipe-fusion products.

Simulations like the one presented in this thesis are useful in the design and development of products in situations where it is impractical or cost-prohibitive to conduct physical experiments. Projects where destructive measurement methods are used, like the measuring the internal fuse temperature of a plastic pipe fitting, benefit greatly from validated simulation tools.

## 4.2 – Future Work

Initial fuses of virgin fittings revealed a sharper and more erratic temperature profile, while all subsequent fuse cycles had a smoother temperature profile. It was determined this was likely due to air gaps between fitting components. The air gaps cause thermal energy to build up in random, localized areas around the susceptor rings. This causes variations in the HDPE thermal expansion, which moves the susceptor rings during the first fuse of a virgin fitting.

Future work could see efforts to fully understand the effect of air gaps through farther analysis of virgin fitting fuses. Variations in HDPE thermal expansion may cause thermocouple movement during an initial fuse, which may be a factor in the erratic temperature measurements found during the first fuse.

The simulation was found to not agree with the first fuse of a virgin fitting. This is due to it not accounting for the air gap phenomenon or the complexities of the HDPE material used in the fitting. The complex semi-crystalline structure of the HDPE polymers causes thermal history affects that affect subsequent heat cycles. This makes accurate simulation extremely challenging. Future work could see efforts to account for more aspects of the HDPE physical complexities.

As mentioned in Appendix F, the $S_{11}$ was seen to change between virgin and non-virgin fittings due to ring movement. More work could be done to verify pre-fuse placement of the susceptor ring sleeve. If the sleeve is pushed passed where it is designed to sit, by slipping over an internal lip of the fitting, then the $S_{11}$ would be thrown off from the start.

The most important future work is to simply use the simulation tool presented in this thesis. This tool has been validated against measurements of the physical TRITON™ 2-inch system and shown to provide reasonable results. Further efforts would see this tool used to aid in the design and development of other TRITON™ products.

# References


[1] O. Lucía, P. Maussion, E. J. Dede and J. M. Burdío, "Induction Heating Technology and Its Applications: Past Developments, Current Technology, and Future Challenges," *IEEE Transactions On Industrial Electronics,* vol. 61, no. 5, 2014.

[2] G. N. P. C. M. D. A Iagăr, "Comparative study between the melting process of an," *Journal of Physics: Conference Series,* no. Series 1781, 2021.

[3] M. H. J.-P. I. Ali YouSsefpour,"Fusion Bonding/Welding of Thermoplastic Composites," *Journal of Thermoplastic Composite Materials,* vol. 17, 2004.

[4] C. Zanini Diego, "MDL," MDL, [Online]. Available: https://tagliotubi-mdl.it/en/welding/ [Accessed May 2023].

[5] S. Pathak and S. K. Pradhan, "Experimentation and optimization of HDPE pipe electro fusion and butt," *Elsevier,* vol. Proceedings 27, p. 2925–2929, 2020.

[6] Fives Group, "INDUCTION WELDING," fives, [Online]. Available: https://www.fivesgroup.com/induction/bonding/welding. [Accessed May 2023].

[7] U.S Department of Commerce National Telecommunicaitons and Information Administration, "nist.gov," January 2016. [Online]. Available: https://www.nist.gov/image/january2016spectrumwallchartpng. [Accessed 22 December 2022].

[8] WATTS, "WATTS," 2013. [Online]. Available: https://www.watts.com/dfsmedia/0533dbba17714b1ab581ab07a4cbb521/26360-source/f-triton. [Accessed February 2023].

[9] WATTS, "WATTS," WATTS, 2022. [Online]. Available: https://www.watts.com/our-story/brands/triton-pipe-fusion. [Accessed March 2022].

[10] A. Y. Miyuki Noguchi, "Volatile and semivolatile organic compound emissions from polymers used," *Heliyon,* vol. 6, no. 3, 2020.

[11] ANSYS, Inc., "DRD Technology," 2011. [Online]. Available: https://static1.squarespace.com/static/56a437f8e0327cd3ef5e7ed8/t/56abd8bbd51cd443cf37b3e7/1454102717403/ansys-hfss-brochure-14.0.pdf. [Accessed 4 2022].

[12] Ansys Inc., "Ansys Mechanical," Ansys, 2023. [Online]. Available: https://www.ansys.com/products/structures/ansys-mechanical. [Accessed 2023].

[13] J. L. I. D. D. v. E. M. Z. U. Matthias C Wapler, "Magnetic properties of materials for MR engineering, micro-MR and beyond," *Journal of Magnetic Resonance,* 2014.

[14] Ansoft Corporation, "University of Maryland Anlage Research Group," 21 June 2005. [Online]. Available: http://anlage.umd.edu/HFSSv10UserGuide.pdf. [Accessed June 2021].

[15] D. Johnson, "Transformers," in *Electric Circuit Analysis*, Englewood Cliffs, New Jersey: Prentice-Hall, 1989, pp. 502-512.

[16] S. Zhang, X. Y. Cao, Y. M. Ma, Y. C. Ke, J. K. Zhang and F. S. Wang, "The effects of particle size and content on the thermal conductivity and mechanical properties of Al2O3/ high density polyethylene (HDPE) composites," *Express polymer letters,* vol. 5, no. 7, p. 581–590, 2011.

[17] Y. A. Cengel, R. H. Turner and J. M. Cimbala, Fundamentals of Thermal-Fluid Sciences, Boston: McGraw-Hill Education, 2016.

# APPENDICES

# Appendix A – Methods Explored to Explain Unexpected Modeling Results

Out-of-the-box simulated results provided unreasonable results, from asymmetric induced currents to non-uniform circumferential temperature after a simulated fuse. Before the changes made to HFSS, as detailed in Chapter 2.1, several methods were explored in an effort to fix the simulation to provide more reasonable results.

The HFSS computational space was explored. This was done by varying the radiation boundary box's size to different ratios of the wavelength, such as λ/2 and λ/6. In addition, a Perfectly Matched Layer (PML) boundary was also investigated. PML is another type of boundary that absorbs stray radiation and limits the computational space to a finite boundary. Changes to the boundaries did not significantly alter the simulated results and did not solve the asymmetries seen, as shown in Table 1.

*Table 1: Summary of computational space variation*

| Computational Space Dimension | RMS Deviation from Symmetric (Watts) 0 = Perfectly Symmetric | Execution Time | Efficiency |
|---|---|---|---|
| <λ/6 | 3.3 | 2 to 4 Hours | 62% |
| λ/6 | 2.8 | 6 to 8 Hours | 62% |
| λ/5 | 2.2 | 6 to 8 Hours | 62% |
| λ/4 (Recommended) | 2.0 | 6 to 8 Hours | 62% |
| λ/2 | 7.1 | 8 to 12 Hours | 62% |
| PML | 4.2 | 14 to 16 Hours | 61% |

It was thought that the modeled fuser wand loop geometry, being approximated as a cylindrical strip, was the cause of the non-uniform issues seen. To explore this, the wand loop was re-designed such that it could provide an even current distribution along the fuser loop. This was also found to provide slightly more uniform circumferential heating but was deemed to only be masking the solver setup issues in HFSS. In addition, the re-designed version was not accurate to the single loop in the physical system.

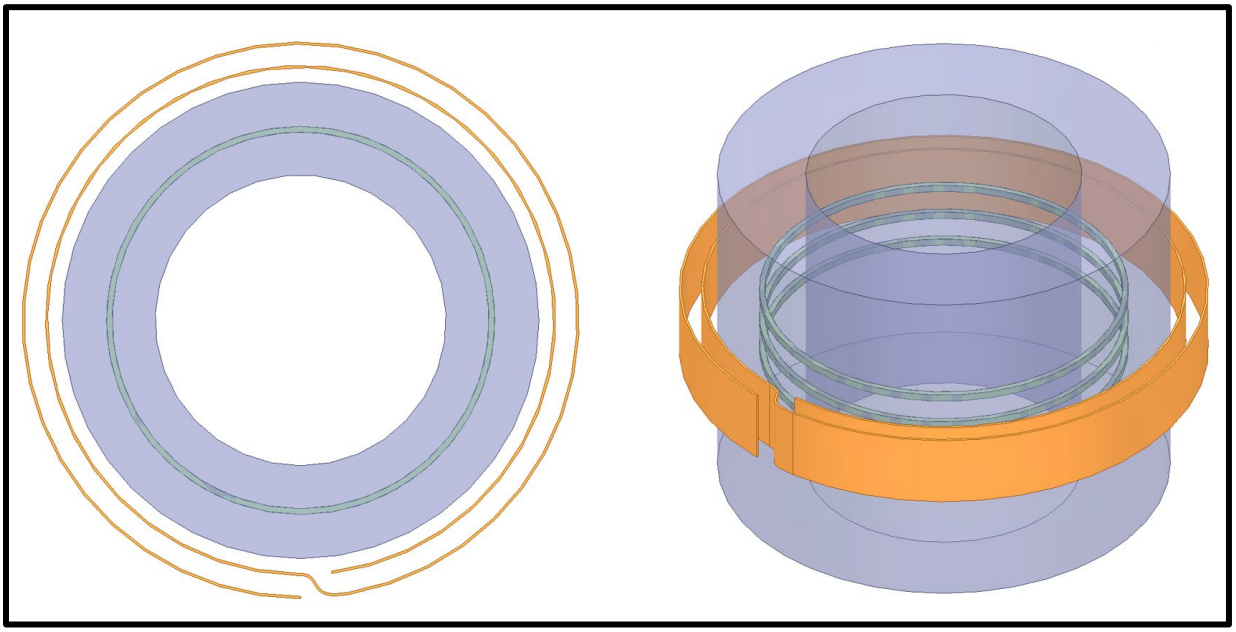

*Figure A35: Fuser wand loop redesign*

The simulated current was set to a defined value during a simulation. Ramping the power, through changes in current values, was explored. Power measurements of the physical system had shown that the power decreases over time as the $S^{11}$ value changes during a fuse cycle. The simulated current was changed to match this power, but it was not found to greatly affect the circumferential asymmetries seen.

## Appendix B – HFSS Simulation Flow Diagram

The HFSS simulation flow is shown below in Figure B36. A full solution pass is performed on the initial mesh geometry. Then, the mesh is refined, and another solution is performed. This repeats until the convergence criteria have been met.

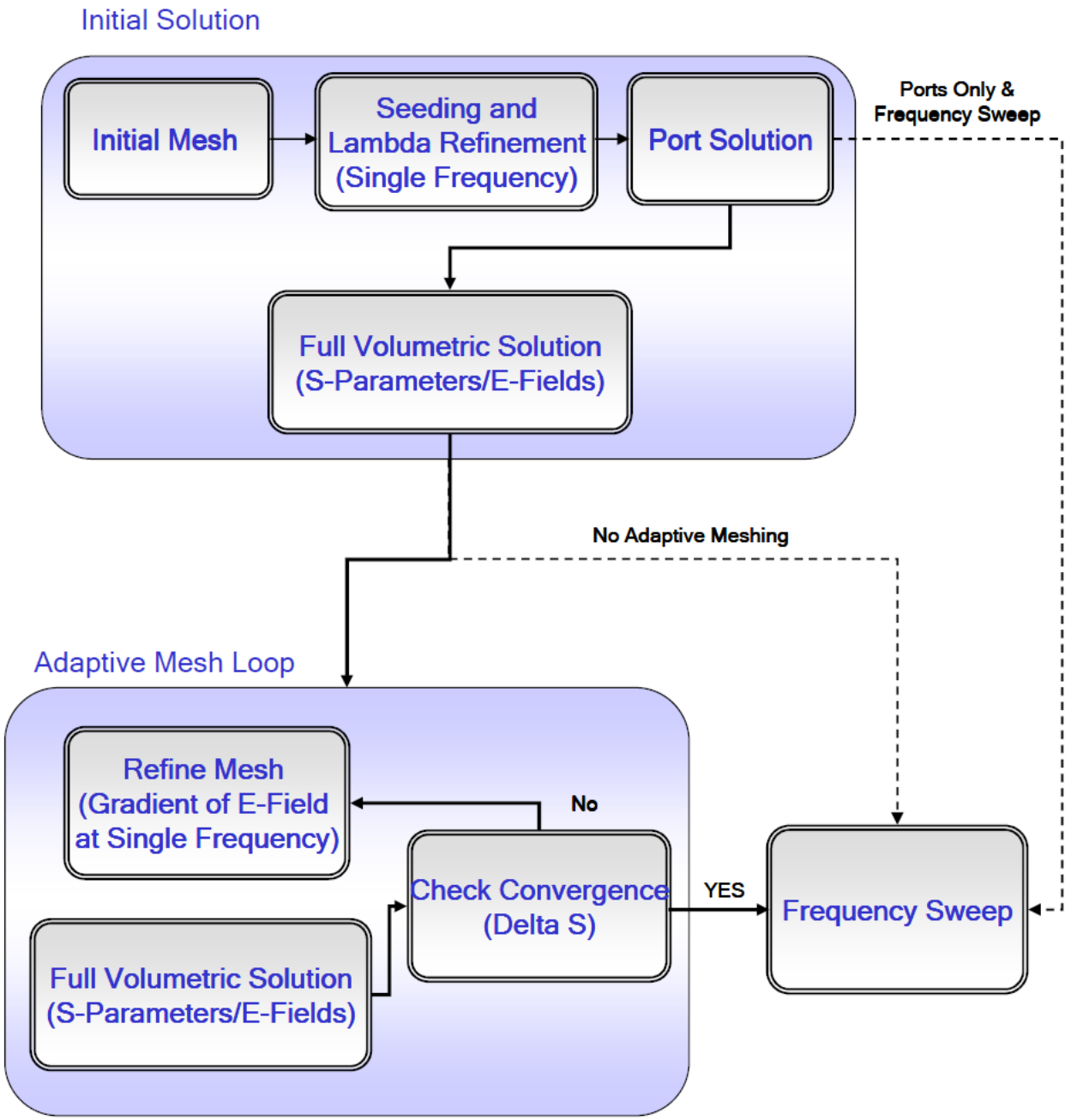


*Figure B36: HFSS Simulation Flow [14]*

## Appendix C – TRITON™ Microprocessor Code Adjustment

Experiments were conducted to collect accurate measurements of the power delivered by the Triton RF Generator to the fusing process. The measurements were carried out using a Bird wattmeter, as well as the RF generator's internal wattmeters. The Triton internal wattmeters are directional couplers that provide both forward and reverse power measurements. The results showed that the internal wattmeters provided measurements similar to the Bird wattmeter, and that the total forward energy delivered to the fusion process was in agreement with what was expected by Watts Water.

The Triton firmware determines how long the RF generator delivers power to the wand, which in turn induces heating in the pipe fitting. The original firmware code was developed by a third-party vendor in the C programming language and was compiled onto a PIC18F2520 microprocessor which controls all aspects of the fusing process. Once initiated, the system measures the standing wave voltage to ensure the fuser wand is connected properly. It then sends power to the wand and measures the energy delivered. The system uses the summed energy amount to determine when to shut off the RF generator.

Using the Bird wattmeter and Triton internal wattmeters, the forward and reflected power to a fuser wand were measured. Ten individual pipe fittings were fused and averaged together, as shown in Table 2. The comparison between the Bird and Triton wattmeters showed close agreement, indicating that the built-in power measurement capability for the RF Generator was working correctly.

*Table 2: Forward and Reflected Power Measurements*

| Time (sec) | FWD Power | REF Power | Accumulated Joules (FWD) | Accumulated Joules (FWD-REF) |
|---|---|---|---|---|
| 5 | 94 | 2.89 | 470 | 456 |
| 10 | 92.6 | 3.67 | 463 | 445 |
| 15 | 91.2 | 3.67 | 456 | 438 |
| 20 | 90 | 4.11 | 450 | 429 |
| 25 | 89.6 | 4.22 | 448 | 427 |
| 30 | 89.2 | 4.67 | 446 | 423 |
| 35 | 88.6 | 4.78 | 443 | 416 |
| 40 | 87.8 | 5.44 | 439 | 412 |
| 45 | 87.4 | 5.56 | 437 | 409 |
| 50 | 87.2 | 5.67 | 436 | 408 |
| 55 | 86.6 | 5.78 | 433 | 404 |
| 60 | 86 | 5.78 | 430 | 401 |
| 65 | 85.6 | 6.11 | 428 | 397 |
| 70 | 85.4 | 6.44 | 427 | 395 |
| 73.3 | 85.4 | 6.44 | 282 | 261 |
| **Total** | | | **6488** | **6123** |

They found the energy delivered to the wand was approximately 6% lower than the expected energy total. They determined the original software calculated energy delivered based on forward power as measured by the Triton internal forward wattmeter. The software did not account for RF reflection from the fuser wand.

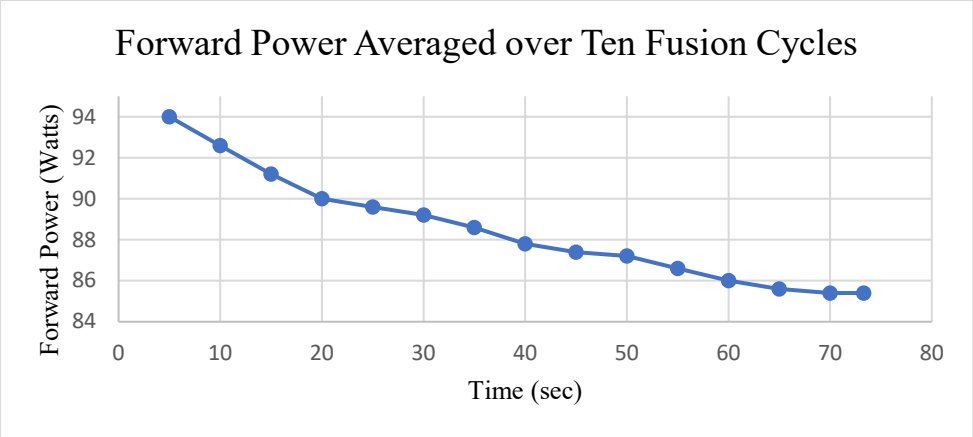


*Figure C37: Average Forward Power Measurement for 3/4" Fitting*

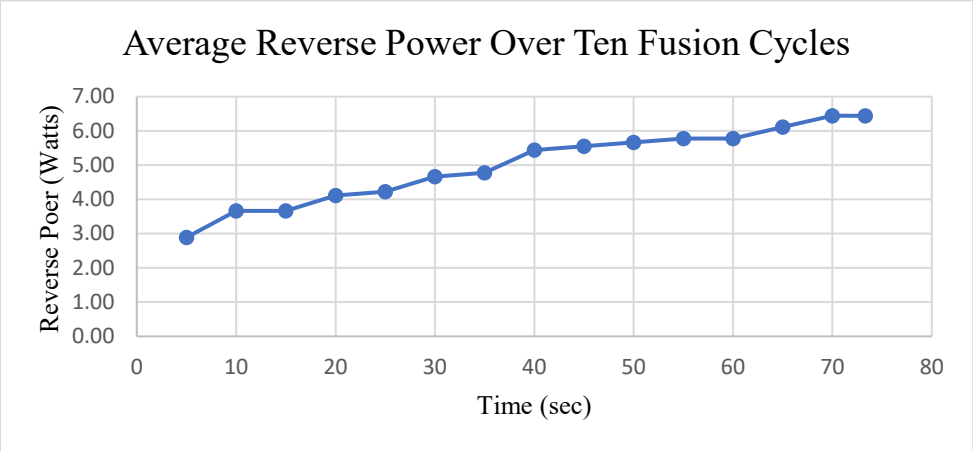


*Figure C38: Average Reverse Power Measurement for 3/4" Fitting*

It was observed that the forward power, plotted in Figure A37 as a function of time, decreased throughout the fuse. The decrease in power was initially thought to be only the components within the generator warming up and becoming more lossy. Similarly, as seen in Figure A38, the reflected power increases with time. It was initially thought the increase in reflected power was due to a mismatch caused by heating in the wand's matching circuit.

A modification to the code was made so the energy delivered to the fusing process compensated for the power reflected by the fuser wand. Following this modification, the forward and reflected power reported by the software, as measured by the directional couplers, were then in agreement with the Bird wattmeter readings.

## Appendix D – Thermocouple Use and Placement

Type-K thermocouple wire was chosen because it covered the thermal range required and spools of the wire were widely available for use. A thermocouple wire welder, such as Figure C39, was used to create thermocouples as needed by welding the end of the two wires that make up a thermocouple. Care was taken to make thermocouple heads as small and identical as possible. This method proved reliable and easily repeatable.


*Figure D39: Thermocouple Wire Welder*

Each thermocouple was used only once to collect fuse temperature data. As such, each thermocouple was expected to output identical results to keep collected data consistent and reliable. A simple experiment was performed to validate the method of using different thermocouples for each fuse. Twelve type-k thermocouples were used to measure ambient room temperature, boiling water, and the surface layer of ice. As can be seen in *Table 3*, the measurement deviation was under 1 degree Celsius. This experiment had shown Type-K thermocouples were repeatable enough to measure the temperature of a fitting during a fuse cycle. A 1°C error was deemed acceptable for this research. It should be noted this experiment's

main purpose was to showcase the difference between thermocouples and not their absolute accuracy. However, the results presented below show the thermocouple accuracy to be consistent with the expected results of each test, farther validating the use of the Type-K thermocouples used in this research application. This experiment also validated the system of measurement used to convert the thermocouple voltage to temperature with the National Instruments 9211 Thermocouple Input Module.

*Table 3: Thermocouple Validations*

| Thermocouple | Ambient Air (°C) | Boiled Water (°C) | Ice (°C) |
|---|---|---|---|
| 1 | 21.7 | 101.3 | 0.1 |
| 2 | 21.8 | 101.2 | 0.1 |
| 3 | 22.3 | 101.5 | 0.1 |
| 4 | 22.3 | 101 | 0.1 |
| 5 | 22.9 | 101.4 | 0.1 |
| 6 | 23.3 | 101.2 | 0.1 |
| 7 | 22.2 | 101.5 | 0.1 |
| 8 | 22.2 | 101.2 | 0.2 |
| 9 | 22.3 | 101.2 | 0.3 |
| 10 | 22.4 | 101.3 | 0.4 |
| 11 | 22.4 | 101.2 | 0.3 |
| 12 | 22.5 | 101.2 | 0.5 |

Before a fuse measurement, HDPE pipes would be rinsed with isopropyl alcohol to remove any potential grease or debris. Then, a fine sandpaper (200-400 grit) was used to rough the pipe end that was inserted into the fitting end.

A caliper was used to measure the wall thickness of the pipe fitting, so a drill bit could be marked to indicate the insertion depth needed to place the head of the thermocouple at the ring, as shown in Figure C40. However, there were several problems with this method. Each measurement and corresponding mark were made by hand, allowing for too much error between each thermocouple placement. Additionally, since the head of a thermocouple is wider in diameter than the rest of the thermocouple, a column of air was left behind the thermocouple head to the surface of the fitting. This was found to also create more variability between thermocouple measurements. Filling the air columns with different pastes, such as thermal paste, did not decrease the variability seen. It was concluded the horizontal method did not produce reliable data.

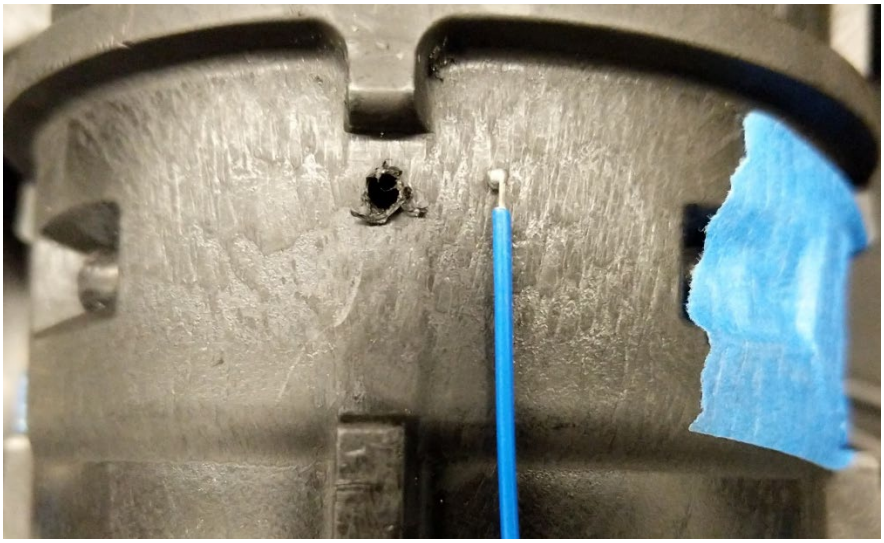

*Figure D40: Horizontal method of thermocouple placement*

The second method explored was to place a thermocouple vertically to the susceptor ring. The first attempt at vertical thermocouple placement was to tape a thermocouple to the susceptor ring sleeve with the head of the thermocouple located at the top ring. The sleeve was then inserted into a pipe fitting with a tapered groove notched in it to accommodate the thermocouple head. The groove narrowed farther into the fitting to help close any potential air gaps. An example can be seen below in Figure C41. The advantage to this method was two thermocouples could be inserted into one fitting which allowed for an electrical continuity check between both thermocouples to ensure they were touching the ring directly. The continuity check was used in the first few experiments to prove the vertical thermocouple method was repeatable.

*Figure D41: Example of vertical thermocouple outside susceptor ring sleeve*

A gradual and smooth heating profile was expected; but, as can be seen in Figure C42, that was not the case. Significant variation in the temperature can be seen in the 120°C to 140°C range. This was seen on other fuse trials as well. A thermocouple was placed on the outside of the fitting to rule out potential interference from the fuser wand loop. No such interference was found. Experiments with Kapton and aluminum tape over the thermocouple were not successful in solving the measurement variation seen. It should be noted the cool down temperature profile was unaffected by what was causing the variance in the heat up profile. It was believed there was

something volatile at the ring which caused the temperature reading to swing more than expected. If the voltage spike was caused by the EMF, it was expected to show on both the thermocouple leads at the same time, creating a common mode voltage that would result in no change in thermocouple reading. The absolute voltage difference would still be measured by the thermocouple input module.

As will be discussed later in this thesis, crystallinity changes of the HDPE allowed material to flow in air gaps around the susceptor ring and thermocouple. This movement caused thermocouples to change position relative to the susceptor ring during a fuse, especially when initially located at the surface of a susceptor ring.

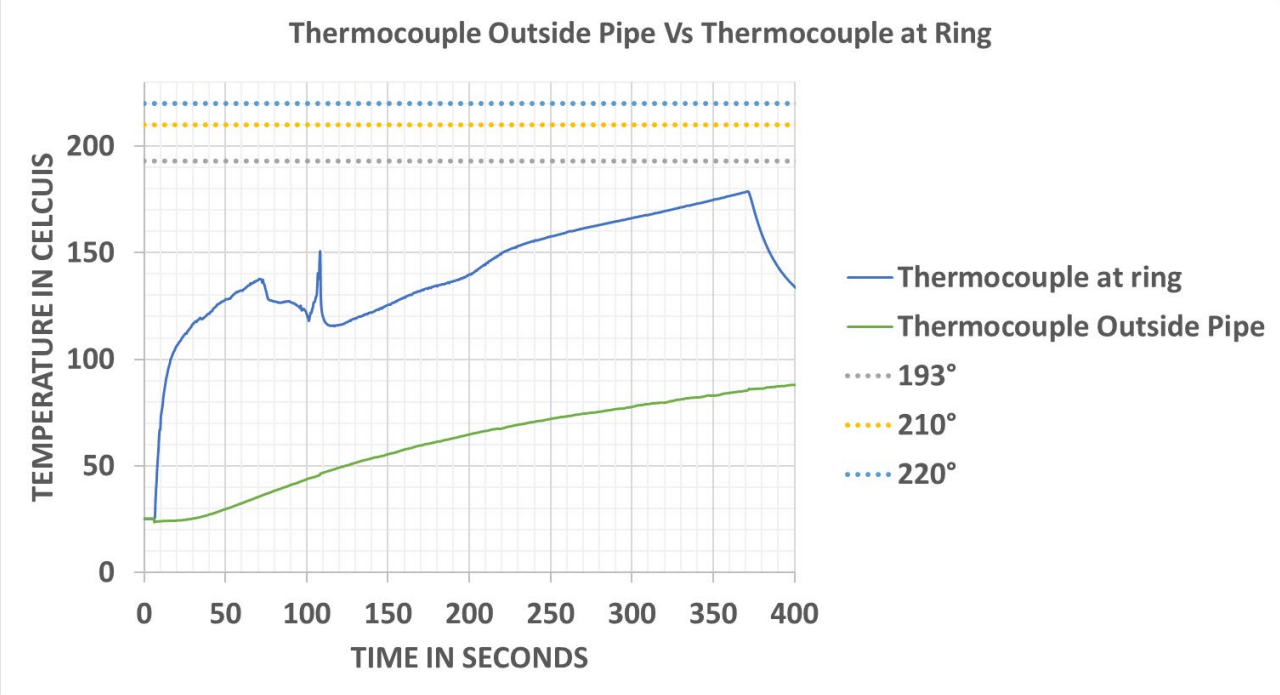


*Figure D42: Measured fuse with thermocouple touching susceptor ring*

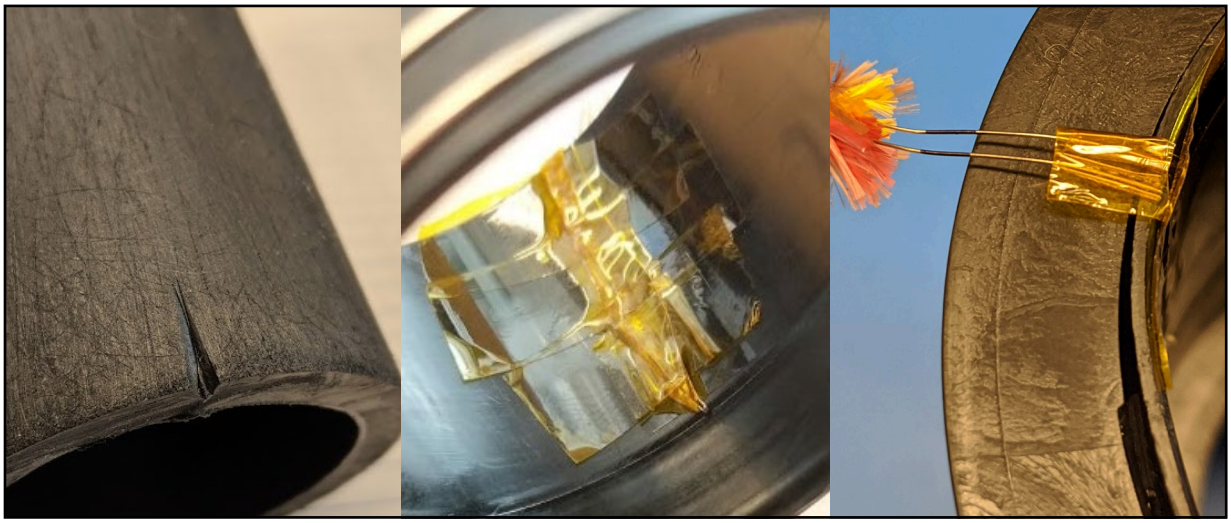

*Figure D43: Example of vertical thermocouple inside susceptor ring sleeve*

To mitigate these effects, the thermocouple was instead taped to the inner surface of the susceptor ring sleeve, shown in Figure C43. Doing so placed approximately 0.33mm of HDPE between the thermocouple and the susceptor ring. The same method of taping the thermocouple down was employed, but care was taken to ensure the pieces of tape were overlaid in such a way to let the pipe slide over them without catching their edges. A notch in the pipe was made to help the pipe not pull the thermocouple down passed the susceptor ring. Marks were made on each thermocouple to indicate potential movement when the pipe was inserted into the fitting.

Offsetting the thermocouple from the variability of the ring proved to be an effective method. Not only did it remove the spike in temperature, as seen previously, but the temperature of measured fuses remained consistent between other fuses The method of placing thermocouples on the inner surface of the susceptor ring sleeve was found to provide the most consistent results.

## Appendix E – HDPE Polymers

HDPE is semi-crystalline polymer with both crystalline and amorphous regions. The crystalline regions have arranged polymer crystals while the amorphous region is random. Each region has varying properties, such as melting point. As HDPE is heated, it undergoes multiple thermal transition regions, which see changes at a molecular level that affect its physical properties. Some of these regions are the Gamma, Betta, and Crystalline transitions. The Gamma transition is due to sub molecular chain reactions that change the crystalline structure. The Betta transition is the glass transition region, which sees the polymers move from a glassy state to a more fluid state. Both transitions are difficult to measure due to the complexity in measuring them independent of the Crystalline transition, which is a $4^{th}$ order discontinuous transition where the crystalline region melts and the amorphous region crystalizes. The two regions have different properties throughout the crystalline transition, which results in a non-linear heat profile. As the HDPE cools, it again passes through the thermal transitions which change the morphological structure of the material. Due to the change in polymer structure, the following heat cycles are slightly varied from the previous cycles. This is commonly called the thermal heat history of the polymer material.

The plot in Figure D44 shows the temperature profile of a sample of HDPE heated in an oven around 210 C. Trial 1 was the first heat cycle and trial 2 was the second heat cycle. It is seen that temperature dependance exists due to the non-linear profile in both the heating and cooling of the sample. Overlaid with the real-world measurements is a simulated thermal profile of an ANSYS Mechanical model of the same heating experiment. The thermal simulator does not account for the temperature dependance seen in the physical sample and is shown to have a smooth heat profile.

Accurately simulating HDPE to real-world measurements is a very challenging task due to the complexity of the semi-crystalline structure of HDPE polymers. With off-the-shelf simulators, like ANSYS Mechanical, the best approach is to fit the simulated results to the measured curve best as possible, without accounting for the phase transitions and thermal conductivity change along the temperature band.

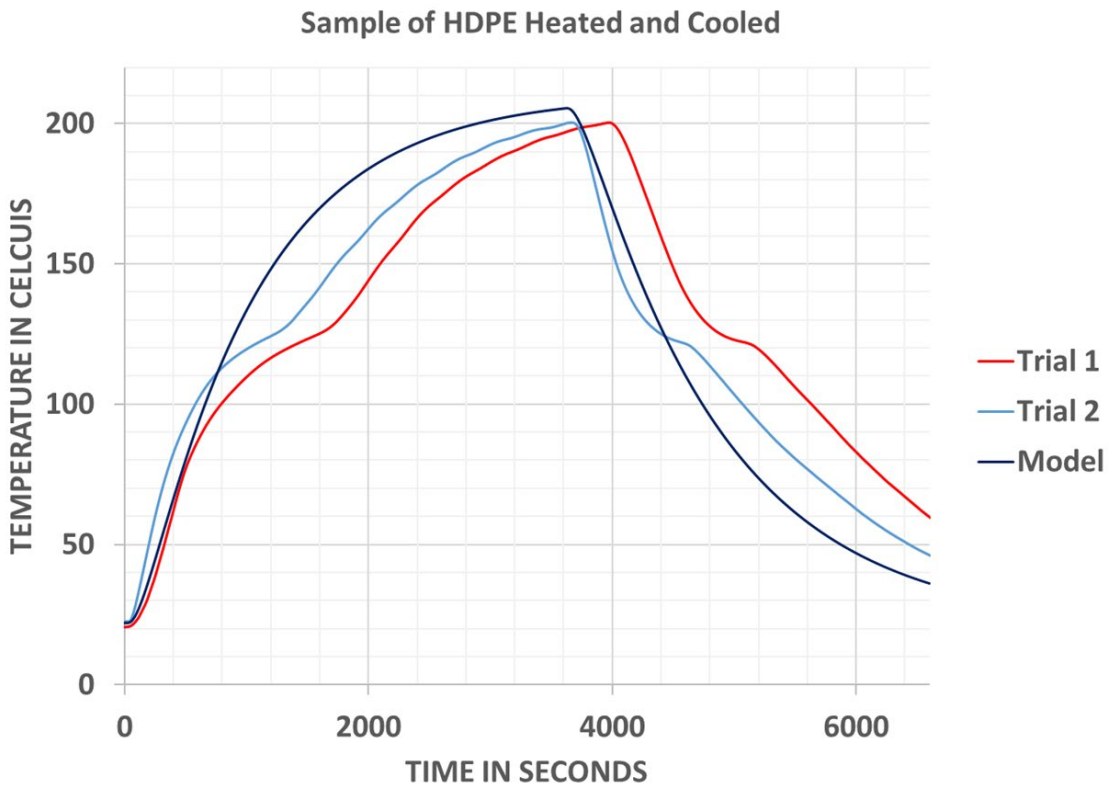


*Figure E44: Measured and Simulated HDPE Heating*

## Appendix F –Circumferential Non-Uniformity Investigation

While collecting fuse temperature profile measurements, it was found that the first fuse cycle for a virgin fitting consistently had a different thermal profile than subsequent fuses on the same fitting. Also, different virgin fittings had varied fuse thermal profiles from each other. Figure G45 shows the temperature profiles of the first fuse cycle for five different virgin fittings.

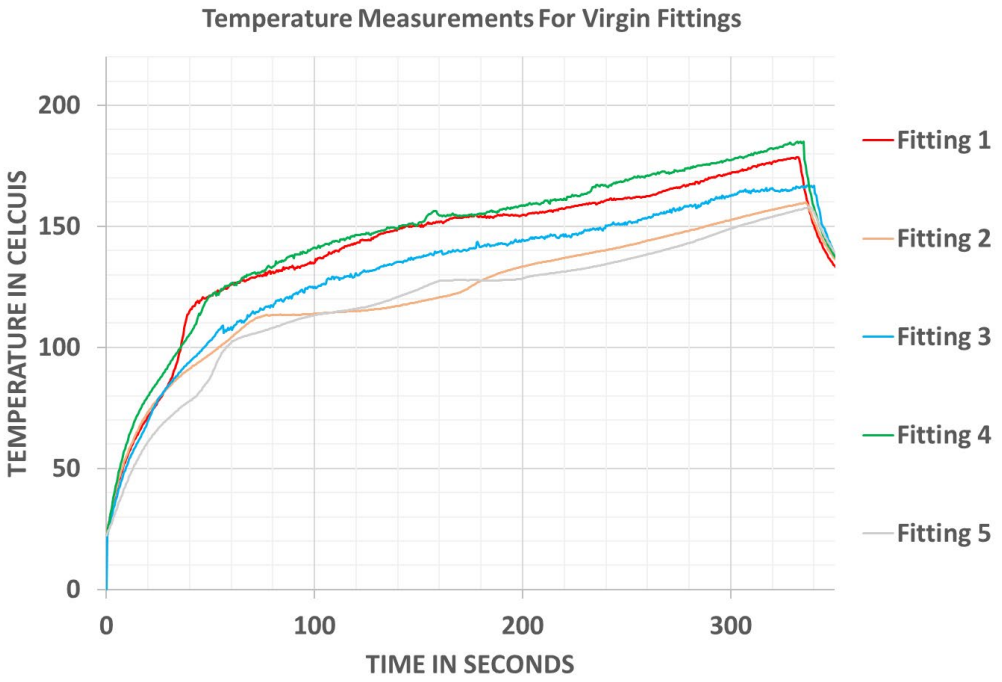


*Figure F45: Thermocouple Fuse Measurement On Virgin Fittings*

To understand the cause of this phenomenon, IR measurements were taken of a fitting during a fuse cycle. The fitting was cut 10mm above the topmost susceptor ring to allow the IR camera to measure the temperature closer to the ring. Figure G46 shows visible air gaps between the susceptor ring sleeve and the pipe fitting as the susceptor ring heats up.

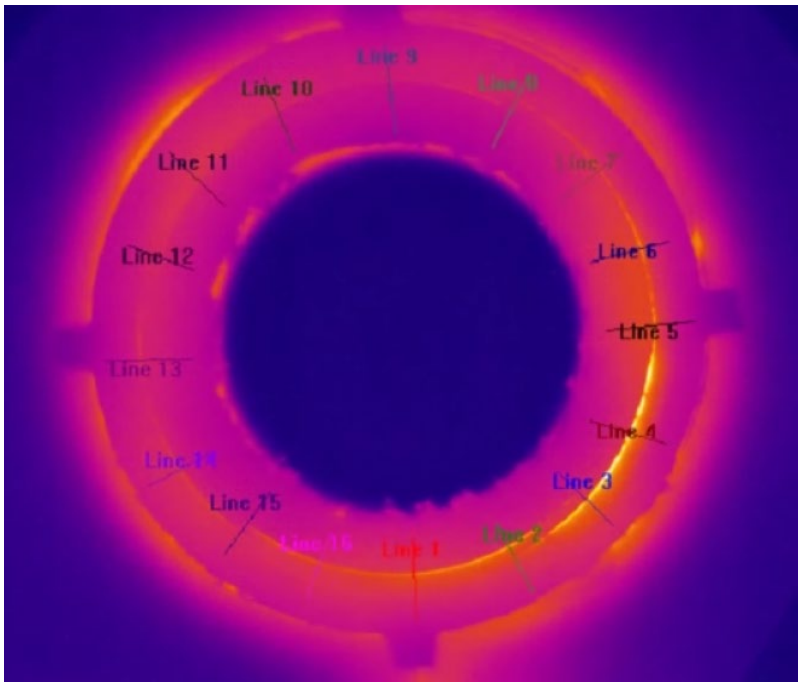


*Figure F46: IR Fuse Measurement Capture 10mm From Susceptor Ring to Top of Fitting*

A second experiment was conducted where the fitting was cut to expose the topmost susceptor ring. The yellow circles in Figure G47(a) show gaps around the susceptor ring. Figure G47(b) shows hot spots during a fuse cycle that correspond with the gaps identified before the fuse in Figure G47(a).

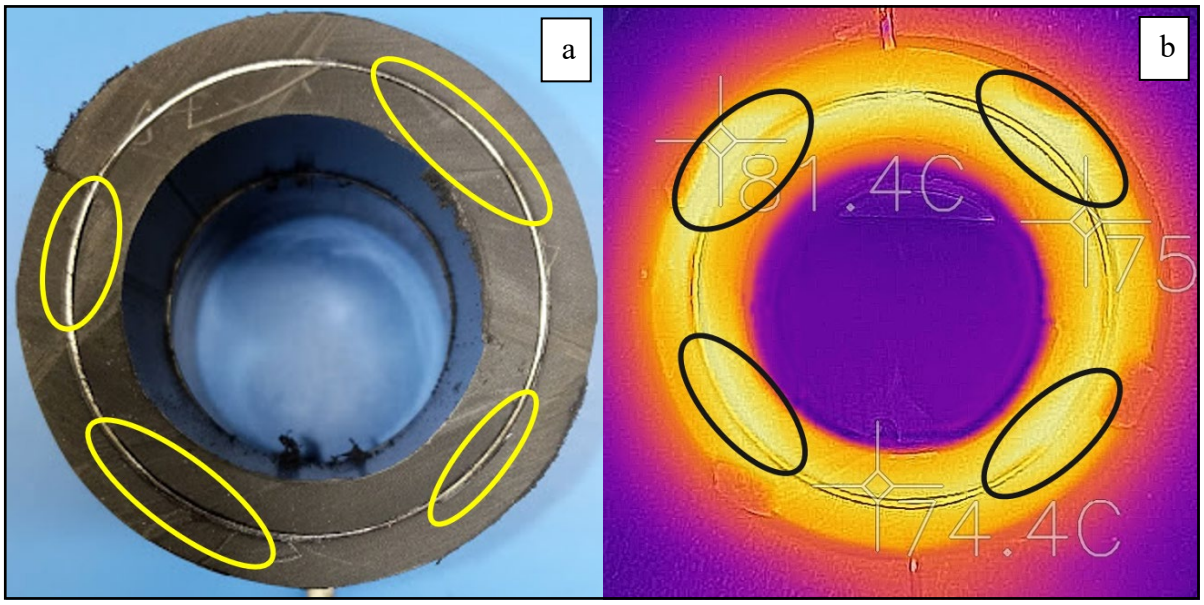


*Figure F47: Visible Air Gaps in Virgin Fitting (a), Hot Spots Measured by IR Camera (b)*

It was hypothesized that the air gaps allow for movement of the susceptor rings during a fuse cycle once the HDPE reaches the crystalline transition phase. HDPE experiences significant thermal expansion during a heat-cycle. Regions of varying temperature would cause variations in HDPE expansion.

This movement was confirmed with µCT scans of susceptor rings before and after a fuse cycle. The position of the fitting with the µCT scanner was precisely controlled. Figure G48 shows the differences between the bottom edges of nearest and farthest points of the ring from a profile view. Similar changes were seen throughout multiple similar experiments. No pattern was found for susceptor rings

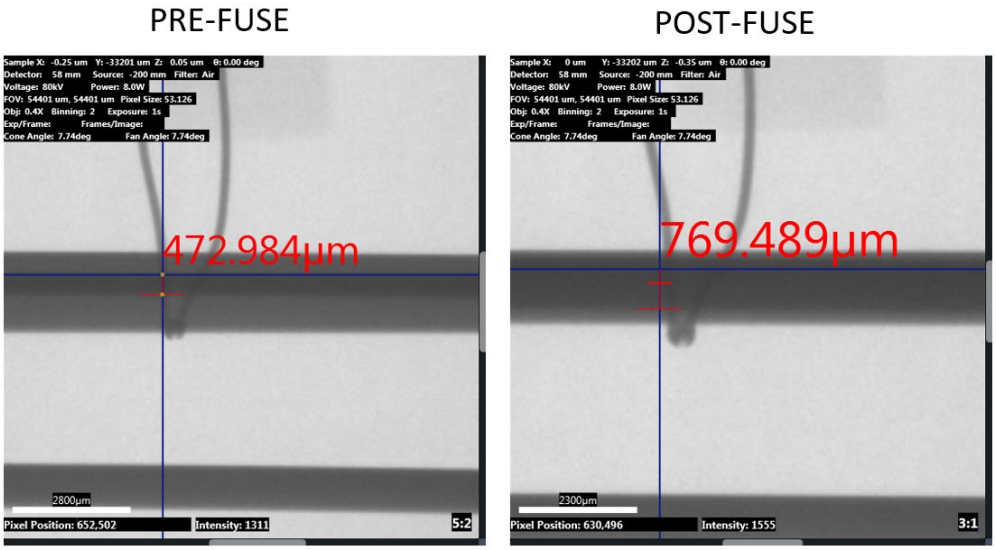


*Figure F48: µCT Images of a Susceptor Ring Before and After a Fuse*

The $S_{11}$ reflection coefficient was also seen to change between virgin and non-virgin fittings. For one fitting, the $S_{11}$ before the fuse was about -46 dB. After the first fuse, and subsequent fuses, the $S_{11}$ was about -23 dB. This change also suggests that there is ring movement during a fuse cycle. Susceptor ring movement would change the inductive coupling between the fuser loop and the rings, thereby changing the $S_{11}$ reflection coefficient.

Air has a much lower thermal conductivity than the HDPE used in the fittings, around 0.03 $\frac{W}{m\,K}$ and 0.4 $\frac{W}{m\,K}$, respectively [15] [16]. The pockets of air around regions of the susceptor ring were thought to trap thermal energy in those localized regions. Thus, it was hypothesized that air gaps around the susceptor rings drive the positive feedback loop formerly described.

A MATLAB simulation of the susceptor ring and surrounding HPDE was constructed to demonstrate the effect of localized heating during a fuse. The simulation partitions the susceptor rings into segments of length $\Delta\ell$. The resistance (R) of each segment is:

$$R_{Segment} = \frac{\Delta\ell}{\sigma A} \tag{8}$$

*Equation G3: Resistance for Each Segment*

where $\sigma$ (S/m) is the conductivity of the susceptor ring and A ($mm^2$) is the cross-sectional area of the ring. The resistance of metals is known to change with temperature (T) according to:

$$R(t) = R_{Ambient}[1 + \alpha(T - T_{Ambient})] \tag{9}$$

*Equation G4: Temperature-Resistance Relationship*

where $\alpha$ is the temperature coefficient of resistance, which describes how the resistance of the ring changes with temperature. The simulation recursively steps through time assuming a constant current (I) across the susceptor ring. At each time step, it calculates the energy delivered to each segment:

$$Energy = \left(I^2 R_{Segment}\right)\Delta T \tag{10}$$

*Equation G5: Energy Delivered to Each Segment*

The segment temperature is raised according to the energy delivered to it, its mass, and its specific heat:

$$\Delta T = \frac{Energy}{mass \times specific\ heat} \tag{11}$$

*Equation G6: Segment Temperature Change*

Based on the measured resistance of a heated susceptor ring (Figure 28), $\alpha$ was derived to be $3.79 \times 10^{-3}$. A validation of the derived $\alpha$ value was conducted using MATLAB. Figure G49 shows the results closely followed measurements of the physical susceptor ring temperature versus resistance.

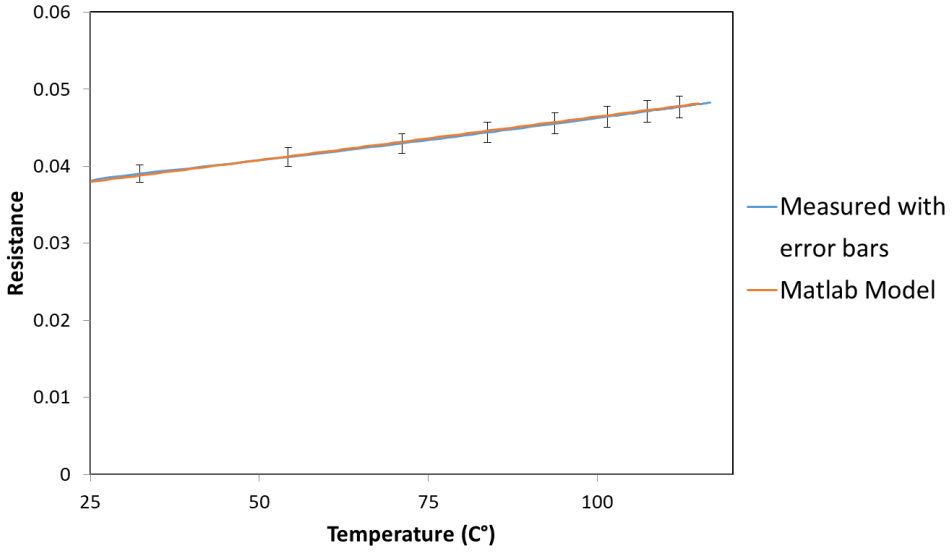


*Figure F49: Measured and Simulated Susceptor Ring Temperature versus Resistance*

A single cell in the MATLAB simulation was set to have lower thermal conductivity to simulate an air pocket. The simulated circumferential thermal profile (Figure G50) indicated that the air gaps result in increased localized heating. This, in turn, increases the resistance of the susceptor rings and provides a positive feedback loop which is the likely cause of the hot spots and fuse temperature profile variability.

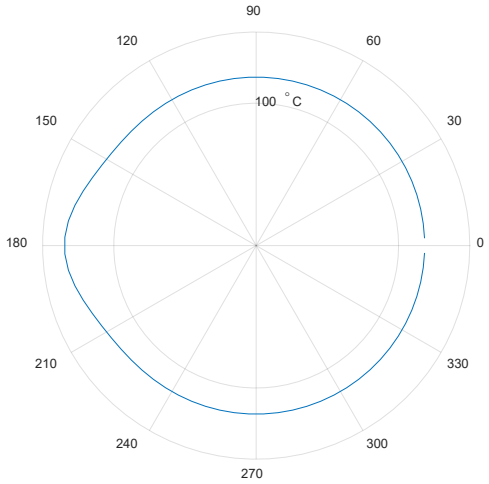


*Figure F50: MATLAB Model with Asymmetrical Heating*

## Appendix G – Transformer Model Representation

The fusing process can be thought of as a transformer where the wand loop acts as the primary coil and the susceptor rings act as the secondary. A standard transformer model was used to show this, as seen in Figure E51.

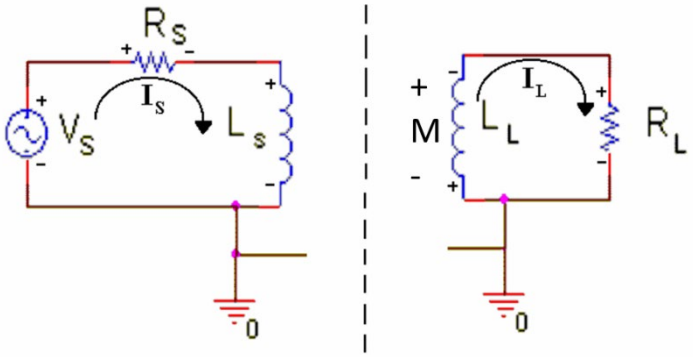


*Figure G51: Standard transformer model circuit [17] used to determine losses in the fusing process*

The loop equation for the load current, $I_L$, can be written as:

$$I_s j\omega M = I_L j\omega L_L + I_L R_L \tag{3}$$

*Equation 7: Loop equation for load current*

where $I_s$ is the source current, $L_L$ is the load inductance, $R_L$ is the load resistance, and $M$ is the mutual impedance. $M$ is equal to $k\sqrt{L_S L_L}$ where $L_S$ is the source inductance and the coupling coefficient, $k$, is defined as $0 \leq k \leq 1$. Rearranging the loop equation yields the ratio between the two currents:

$$\frac{I_L}{I_S} = \frac{j\omega M}{j\omega L_L + R_L} \tag{4}$$

*Equation 8: Ratio between two currents*

From this ratio, the total power dissipated in the wand and the susceptor rings ($P_{Total}$) can be determined in terms of the source current:

$$P_{Total} = {I_S}^2(NR_S) + {I_L}^2 R_L = {I_S}^2(NR_S) + {I_S}^2 \left(\frac{j\omega k\sqrt{(NL_S)L_L}}{j\omega L_L + R_L}\right)^2 R_L \quad (5)$$

*Equation 9: Total power dissipated in the wand and susceptor rings in terms of source current*

where *N* is the number of turns on the wand loop, and $R_S$ is the source resistance. Based on this equation, the efficiency is given by:

$$Efficiency = \frac{P_{susceptor}}{P_{Total}} = \frac{{I_L}^2 R_L}{{I_S}^2(NR_S) + {I_S}^2\left(\frac{j\omega k\sqrt{(NL_S)L_L}}{j\omega L_L + R_L}\right)^2 R_L} = \frac{{I_S}^2\left(\frac{j\omega k\sqrt{(NL_S)L_L}}{j\omega L_L + R_L}\right)^2 R_L}{{I_S}^2(NR_S) + {I_S}^2\left(\frac{j\omega k\sqrt{(NL_S)L_L}}{j\omega L_L + R_L}\right)^2 R_L} \quad (6)$$

*Equation 10: Efficiency*

which can be further simplified to:

$$Efficiency = \frac{\left(\frac{j\omega k\sqrt{L_S L_L}}{j\omega L_L + R_L}\right)^2 R_L}{R_S + \left(\frac{j\omega k\sqrt{L_S L_L}}{j\omega L_L + R_L}\right)^2 R_L} \quad (7)$$

*Equation 11: Efficiency simplified*

One interesting conclusion that can be drawn from *Equation 11* is the number of turns on the wand loop cancels out. Thus, the efficiency will remain unchanged if more turns are added to the wand loop. This remains true if the resistance of the loop stays the same. However, adding extra turns without reducing the size of the loop conductor will increase its resistance and therefore decrease efficiency.

The values of inductance used in the simulation were determined from measurements. Those values were used to approximate the coupling coefficient, *M,* to be 0.96. This value for *M* seemed reasonable since the HFSS model indicated 4% of the energy was radiated. In the 2-inch fitting model, the two outer susceptor rings are closer to the edge of the wand loop and

experience the highest magnetic flux. Since the transformer model is a circuit model, its conductance is given in Siemens [mhos or ohm$^{-1}$] while the conductivity in the HFSS full-wave model is given in Siemens/meter. Thus, the HFSS model results presented in Figure 26 should not be compared directly to the mathematical model, but rather used to display the trends between the two models.

Figure E52 shows the calculated efficiency for the transformer model as a function of secondary loop resistance.

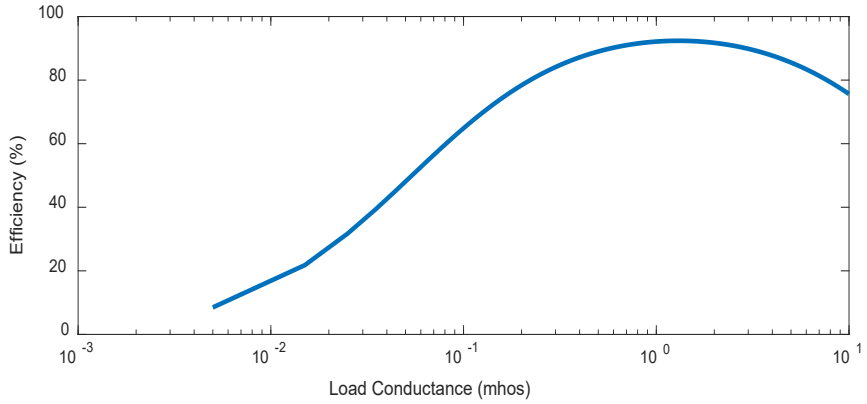


*Figure G52: Modeled efficiency for the transformer model as a function of secondary loop conductance.*

As expected, both the transformer and HFSS models show an efficiency trending towards zero for both very high and very low conductivities.

## Appendix H – Susceptor Ring Resistance Versus Temperature

In Figure F53, below, the resistance of a susceptor ring is shown during a high current resistance measurement. During the measurement, air was blown across the ring. The high air convection removed thermal energy from the ring, which in turn lowered the electrical resistance of the ring.

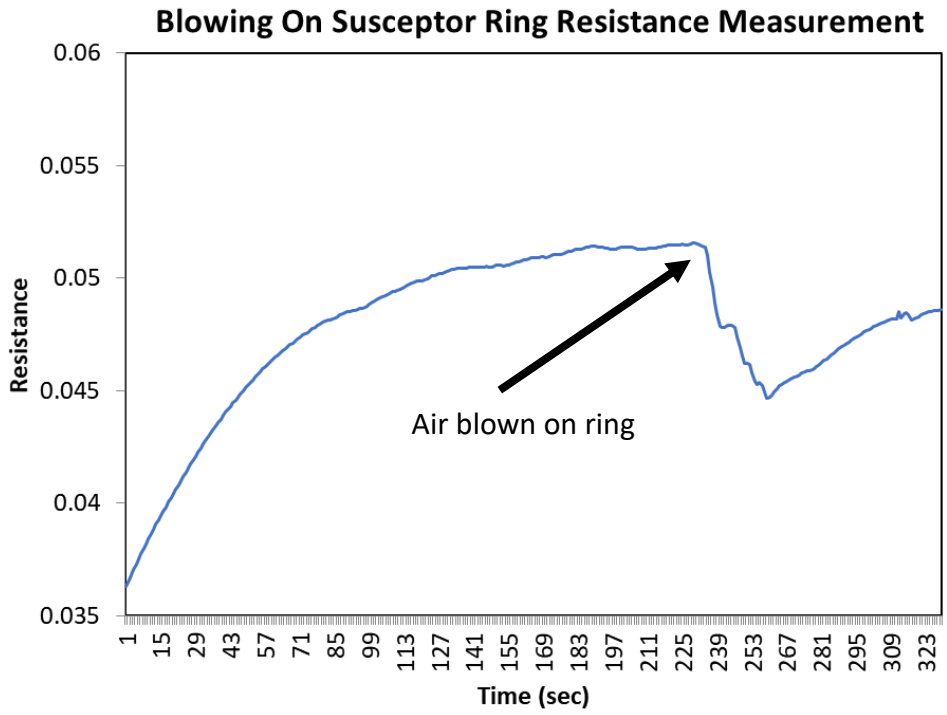


*Figure H53: Higher Convection During Measured Susceptor Ring Resistance*